

H2020 FETHPC-1-2014



Enabling Exascale Fluid Dynamics Simulations
Project Number 671571

D3.1 - Detailed Description of Use Cases and their Requirements

WP3: Validation & Case Studies



Copyright© 2015 The ExaFLOW Consortium

The opinions of the authors expressed in this document do not necessarily reflect the official opinion of the ExaFLOW partners nor of the European Commission.

DOCUMENT INFORMATION

Deliverable Number	D3.1
Deliverable Name	Detailed Description of Use Cases and their Requirements
Due Date	31/05/2016 (PM 8)
Deliverable lead	University of Southampton
Authors	Christian T. Jacobs (University of Southampton) Neil D. Sandham (University of Southampton) Nico De Tullio (University of Southampton) Michael R. Bareford (University of Edinburgh) Adam Peplinski (KTH) Ricardo Vinuesa (KTH) Nicolas Offermans (KTH) Philipp Schlatter (KTH) Julien F. A. Hoessler (McLaren) Sridar Dhandapani (McLaren) Jean-Eloi W. Lombard (Imperial College London) Spencer J. Sherwin (Imperial College London) C. J. Falconi D. (ASCS) D. Lautenschlager (Adam Opel AG)
Responsible Author	Christian T. Jacobs (University of Southampton) e-mail: C.T.Jacobs@soton.ac.uk
Keywords	simulations, use cases, requirements, performance, evaluation
WP	WP3
Nature	R
Dissemination Level	PU
Final Version Date	31/05/2016
Reviewed by	Jing Zhang (Univ. Stuttgart/HLRS), Nick Johnsson (Univ. Edinburgh/EPCC)
MGT Board Approval	31/05/2016

DOCUMENT HISTORY

Partner	Date	Comment	Version
University of Southampton	30/04/2016	Initial draft	0.1
University of Southampton	18/05/2016	Updates from internal review	0.2
KTH	31/05/2016	Final version after PMB review	1.0

Executive Summary

This document presents a set of five use cases designed to test the efficiency of the algorithms developed and implemented throughout the ExaFLOW project. The use cases fully exercise the new capabilities built into the various codes developed by the project partners, and can also help expose any potential issues relating to the path to exascale computing. The use cases feature simulations of a jet in crossflow, both incompressible and compressible flow past a NACA4412 airfoil, an automotive simulation, and flow past various aspects of a race car such as the Imperial Front Wing design. Each use case is written by the associated project partner. Due to the length of each use case's description and the wide variety of application areas, each use case is presented as a stand alone document.

<i>D3.1: Detailed Description of Use Cases and their Requirements</i>	5
---	---

Contents

1 Introduction	6
2 Conclusions and Future Work	6
Use Cases 1 & 2: Jet in crossflow & NACA4412 airfoil in incompressible flow	7
Use Case 3: NACA4412 airfoil in compressible flow	19
Use Case 4: Automotive use case	30
Use Case 5: Imperial Front Wing and related cases	38

1 Introduction

Work package (WP) 3 concentrates on analysing the efficiency of the methods developed in WP1 and implemented in WP2 through a set of synthetic and real-world benchmarks/use cases. The use cases have been chosen according to the requirements from our industrial partners to ensure that the project will have impact both in academia and industry. In this document, five such use cases will be presented, namely:

- Jet in crossflow (KTH Royal Institute of Technology)
- NACA4412 airfoil in incompressible flow (KTH Royal Institute of Technology and University of Stuttgart)
- NACA4412 airfoil in compressible flow (University of Southampton)
- Automotive use case (Automotive Simulation Center Stuttgart and Adam Opel AG)
- Imperial Front Wing and related cases (Imperial College London and McLaren Racing Limited)

The use cases fully exercise the various codes and expose known issues relating to exascale computing. This includes the basic algorithms as well as practical aspect such as grid adaptation, I/O and boundary conditions. The test cases have defined quantitative outputs such that changes in the code do not lead to changes in the flow physics. They are also flexible in terms of core counts to allow for weak and strong scaling checks.

Each use case is presented in its own stand-alone document which can be found at the end of this report. Note that the jet in cross-flow and incompressible NACA-4412 use cases are both being considered primarily by the incompressible Nek5000 code and development team, and are therefore presented together in the same document to minimise duplication of background details concerning the code, numerical algorithms and simulation setup guidance. Note that, in addition to Nek5000, the use cases consider the SBLI, Nektar++, and ANSYS Fluent software packages.

2 Conclusions and Future Work

The creation of the five use cases detailed here will facilitate the evaluation of the algorithmic developments and their implementation across the range of codes used in the ExaFLOW project. Preliminary results have been promising, and future work will focus on the continued evaluation of the algorithms using these challenging use cases. An initial evaluation of the WP1 work that will feature the use cases presented here will be presented as part of Deliverable 3.2 at PM 24.

ExaFLOW use cases for Nek5000: incompressible jet in cross-flow and flow around a NACA4412 wing section

A. Peplinski¹, R. Vinuesa¹, N. Offermans¹ and P. Schlatter¹

¹*Linné FLOW Centre and Swedish e-Science Research Centre (SeRC), KTH Mechanics
Osquars Backe 18, SE-100 44 Stockholm, Sweden*

1 Introduction

In this document we present simulation setups that will be used within the ExaFLOW project to test Nek5000 in terms of code development. We will consider two main configurations: jet in cross-flow and incompressible flow around a NACA4412 wing section.

The so-called jet in cross-flow (JCF) refers to a configuration in which fluid exits a nozzle and interacts with a boundary layer developing over a flat plate (Figure 1). This case has been extensively studied both experimentally and theoretically over the past decades due to its high practical relevance. It is also considered a canonical flow problem with complex, fully three-dimensional dynamics which makes the JCF a perfect tool for testing numerical methods and simulation capabilities. Recent reviews on this flow configuration are given in Karagozian (2010), Mahesh (2013). Part of this setup is an inflow pipe, which for some tests will be treated separately.

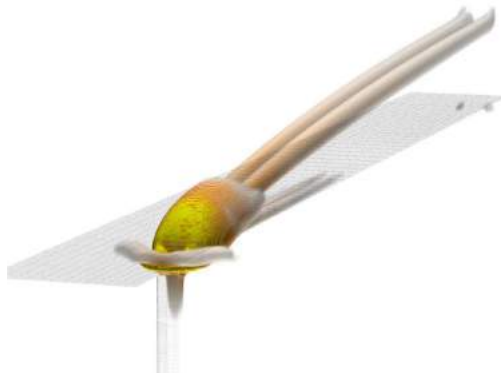


Figure 1: Vortical structures (λ_2 isolevels Jeong & Hussain (1995)) of the base flow for JCF setup including the pipe.

The second configuration under consideration is the incompressible flow around a wing section, represented by a NACA4412 profile. This is an extremely interesting flow case due to the various interacting phenomena present in wings, as observed in Figure 2: laminar-turbulent transition, wall-bounded turbulence under pressure gradients, flow separation and turbulent wake flow. Whereas previous numerical studies of flow around

wings included low-order direct numerical simulations (DNSs) Rodriguez et al. (2013) and large-eddy simulations (LESs) Alferez et al. (2013), as well as high-order DNSs at low Reynolds numbers Shan et al. (2005), we have recently completed a high-order DNS Vinuesa et al. (2015) at an unprecedented Reynolds number of $Re_c = 400,000$ (where Re_c is defined in terms of freestream velocity U_∞ and chord length c). Since a wider scale separation is observed at progressively higher Reynolds numbers, the computing requirements increase dramatically, especially at Reynolds numbers representative of those in academic wind tunnel tests, *i.e.*, from 400,000 up to 1 or 2 million. Hence, this configuration is an excellent test case to evaluate the performance of the various algorithmic developments envisioned in the ExaFLOW project, and to benefit from Exascale capabilities.

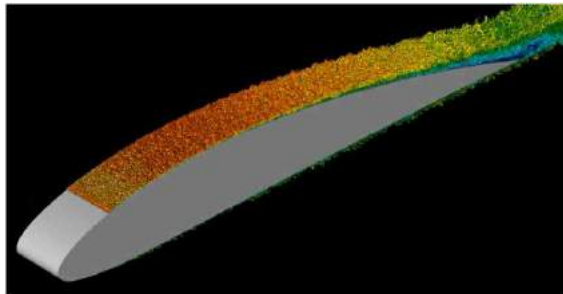


Figure 2: Turbulent structures identified by means of isocontours of the λ_2 criterion Jeong & Hussain (1995) extracted from the NACA4412 wing case.

2 Numerical algorithm

The incompressible Navier-Stokes equations are solved using a spectral element method (SEM) implemented in Nek5000 Fischer, Lottes & Kerkemeier (2008), Fischer & Patera (1994), which is an open-source code developed at the Argonne National Laboratories (Chicago, USA). In SEM the computational domain is decomposed into a set of non-overlapping, high-order, hexahedral sub-domains (elements), where the governing equations are cast into weak form and discretised in space by the Galerkin approximation. C^0 continuity of the variables at the element faces is enforced by direct stiffness summation. Following the $\mathbb{P}_N - \mathbb{P}_{N-2}$ approach the velocity and pressure spaces are locally (within element) spanned by Lagrange polynomial interpolants of order N and $N - 2$ respectively. To ensure flow incompressibility pressure correction scheme is used with the preconditioner based on the additive Schwarz method Fischer (1997). Time integration is based on a generalised BDF k /EXT k scheme. Other discretisation and time integration methods are implemented in Nek5000 as well (*e.g.* $\mathbb{P}_N - \mathbb{P}_N$ and characteristics), however for the ExaFLOW project we will focus on the approach described above.

3 Parallel scaling

Nek5000 is parallelised using the message passing interface (MPI) library. It utilises the natural parallelism of the SEM distributing elements between processors and per-

forming direct stiffness summation in parallel. Parallel performance is improved by use of specialised coarse-grid solvers based on projection scheme (XXT) or algebraic multi-grid (AMG) Fischer, Lottes, Pointer & Siegel (2008). Nek5000 has demonstrated scalability on more than one million ranks, with as few as 5000 grid points per process Fischer, Lottes & Kerkemeier (2008). Results of strong scaling tests of Nek5000 in a number of distributed memory systems are presented in Figure 3.

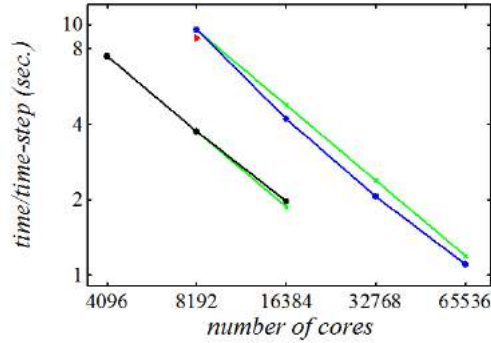


Figure 3: Wall time per time-step for a fixed problem size as a function of number of cores; runs on the systems HECToR (EPCC Edinburgh, UK; ●), Triolith (NSC, Sweden; ●) and Lindgren (PDC, Sweden; ►). Green line shows the linear scaling. The test case is the turbulent pipe flow described below in Table 1, case 3, with a total of 2.2 billion grid points.

4 Standard input/output

The set of required files to start a simulation consists of `###.rea`, `###.re2`, `###.restart` and `rs8###0.f0000i`, where `###` denotes the corresponding setup name (`jet_crf` for JCF and `naca_wing` for flow around NACA4412 wing section) and $i = 1, 2, 3, 4$. `###.rea` contains the simulation parameters, organised in the following sections:

- real parameters
- passive scalar data
- logical parameters
- mesh description
- restart conditions
- history points
- output specifications

`###.re2` is a binary file containing mesh structure and boundary condition information. The initial condition is stored in the set of files `###.restart` and `rs8###0.f0000i`. A

comprehensive description of configuration files and runtime parameters can be found at http://nek5000.github.io/NekDoc/Nek_users.html.

In the JCF case two additional files are required: `hpts.in` (storing positions of velocity probes) and `###.upar` (containing user-defined parameters). `###.upar` has following structure:

```
&USERPAR      ! probe writing frequency
  UPRMPRB= 50,
  /
&CHKPOINT     ! checkpoint parameters
  CHKPTSTEP= 50000,
  IFCHKPTRST=F,
  /
```

The simulation output consists of the instantaneous velocity fields saved as `###n.f0000i` (binary files). In the case of the wing, additional binary files with the format `stat000i` are generated, which correspond to turbulence statistics at a number of locations around the wing. In addition to this, it is also possible to use probes to store time histories of various quantities (such as velocity and vorticity components or pressure). The binary files containing the output of the time history series have the format `pts###n.f0000i`.

5 Jet in cross-flow

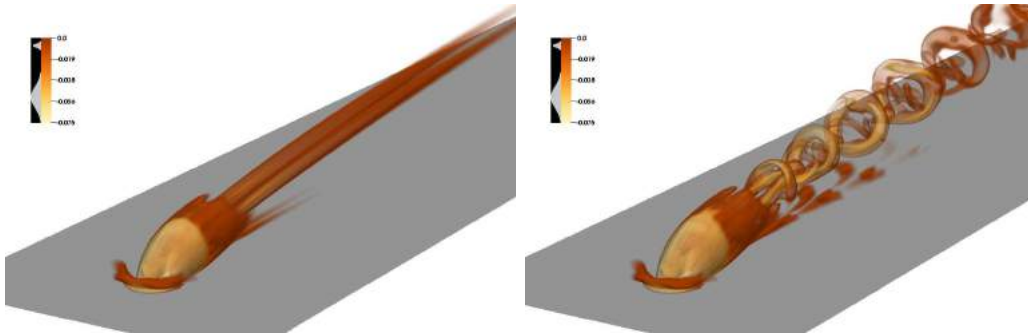


Figure 4: Vortical structures (λ_2 isolevels Jeong & Hussain (1995)) of the JCF for the steady configuration (left) and a periodic vortex shedding (right). Results of the simplified JCF setup without the pipe.

The JCF is characterised by three independent non-dimensional parameters: free-stream Reynolds number ($Re_{\delta_0^*}$), pipe diameter D and jet to free-stream velocity ratio R . As the ratio R increases, the flow evolves from a stable (and thus steady) configuration consisting of (steady) counter-rotating vortex pair (CVP) and horseshoe vortices (left panel in Figure 4), through simple periodic vortex shedding (a limit cycle; right panel in Figure 4) to more complicated quasi-periodic behaviour, before finally becoming turbulent.

In our simulations we consider a circular perpendicular pipe attached to the flat plate (Figure 1) with diameter $D = 3\delta_0^*$, where δ_0^* is the displacement thickness at a position

$7.124\delta_0^*$ upstream from the centre of the pipe orifice (note that δ_0^* is adopted as length unit). The free-stream Reynolds number is $Re_{\delta_0^*} = 200$ and the velocity ratio R is chosen to be close the first bifurcation (between 0.62 and 0.67) making the flow sensitive to the mesh modifications.

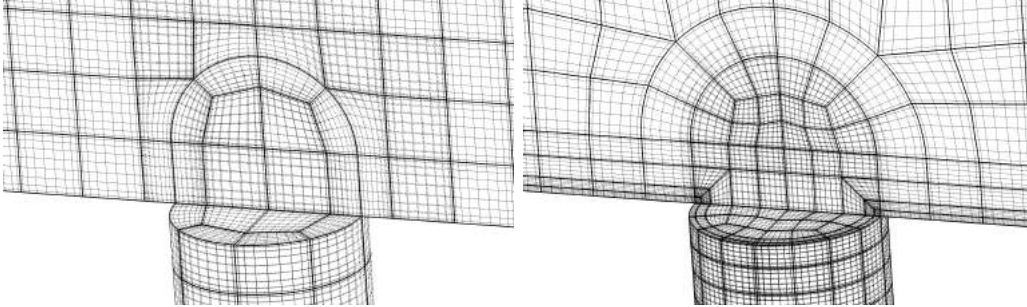


Figure 5: Low (left) and high (right) resolution meshes for JCF. In this Figure we show the mesh structure at the connection between the circular pipe and the rectangular box. The boundaries of the spectral elements are represented by thick lines, whereas the thin ones show the location of the Gauss–Lobatto–Legendre (GLL) points within elements.

The computational domain is composed of a rectangular box and a circular pipe. The mesh structure at the connection between both parts is shown in Figure 5. The size of the rectangular box is set to $L_x = 150$, $L_y = 20$, $L_z = 30$ and is periodic in the spanwise direction. The resolution in this part of the domain is not uniform and we use domain decomposition into elements to reduce the total number of grid points where high resolution is not needed. We keep highest resolution (smallest elements) in the orifice vicinity, and reduce it at larger distances by smooth element stretching. The pipe centre is located 30 units downstream the cross-flow inflow. To investigate the efficiency of adaptive mesh refinement we use number of meshes with different element structure at the pipe inlet but similar resolution at the far field (two examples presented in Figure 5). The lower resolution mesh (left in Figure 5) will be the subject of mesh adaptation, and the high resolution one (right in Figure 5) will provide a reference solution for correctness checks. An additional parameter to control the resolution in the whole domain is the polynomial order N , which will vary from 5 to 11. The total number of grid points will vary between simulations, since the total number of elements and the local polynomial order will be a subject of adaptation.

In our simulations we concentrate on the stability of JCF investigated by linear and non-linear impulse response. In this case we start from evaluation of the steady state for given mesh and parameter set using Selective Frequency Damping. Next we add perturbation to the steady state and measure an amplitude of the strongest mode in the perturbed field. Its time evolution allows us to calculate the mode growth rate, which is a parameter defining linear stability of the system and error measure for our AMR implementation. Figure 6 gives time evolution of the amplitude of the strongest mode for different velocity ratios R with fixed polynomial order $N = 5$ (left panel) and variable N with fixed $R = 0.65$ (right panel). All presented the simulations were performed on low resolution mesh with low amplitude white noise added as perturbation at time $t = 100$. The initial transient growth is clearly visible and is followed by exponential decay (stable

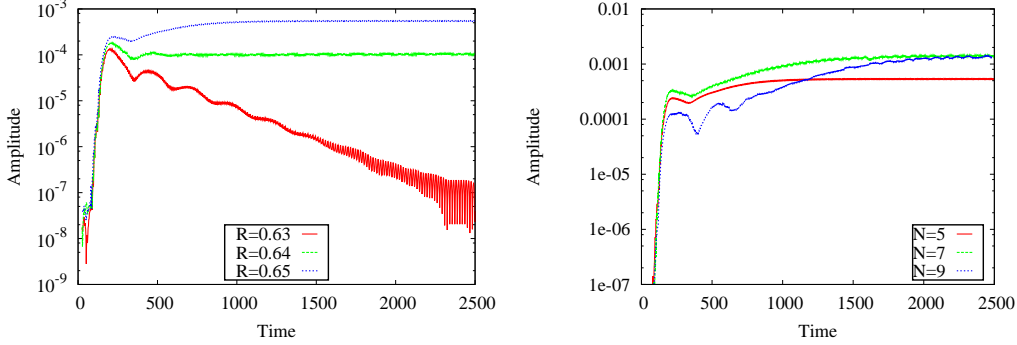


Figure 6: Time evolution of the amplitude of the strongest mode for different velocity ratio R with fixed polynomial order $N = 5$ (left). Right panel shows resolution study for $R = 0.65$ and N ranging from 5 to 9. The transient growth followed by exponential decay/growth phase are clearly visible. For $N = 5$ the bifurcation point is located at $R = 0.64$.

system) or growth (unstable system). Right panel in Figure 6 shows dependency of the growth rate on the mesh resolution, which makes this setup good test case for AMR.

5.1 Turbulent pipe flow

An integral component of the jet in cross-flow configuration, *i.e.*, the turbulent flow through a straight pipe, will be analyzed independently in some of the cases. This is due to the geometrical simplicity of the pipe, which will allow to perform certain tests more easily than in the full JCF setup. A total of three pipe cases are considered, at friction Reynolds numbers Re_τ (based on pipe radius and friction velocity $u_\tau = \sqrt{\tau_w/\rho}$, where τ_w is the wall shear stress and ρ the fluid density) of 180, 550 and 1,000, as summarized in Table 1. The idea is to perform DNSs on the three cases, the first one being aimed at small tests, whereas the remaining two will be used for larger scale runs. Available scaling tests for this configuration can be found in Figure 3. A detailed view of the computational mesh from case 2 is shown in Figure 7, and instantaneous visualizations of the streamwise velocity from cases 2 and 3 can be observed in Figure 8. Note that in all cases a length of $25R$ is considered in the periodic streamwise direction, which is long enough to capture the largest turbulent scales. A complete description of the pipe flow setup can be found in El Khoury et al. (2013).

Case #	Simulation	Re_τ	# grid points
1	DNS	180	19×10^6
2	DNS	550	437×10^6
3	DNS	1,000	2.2×10^9

Table 1: Summary of pipe cases for ExaFLOW project

The strong scaling of the turbulent pipe flow has been performed on several supercomputers for all the Reynolds numbers previously presented. The results for the case $Re_\tau = 550$ on the Cray-XC40 computer “Beskow” at PDC (KTH) are shown in Figure

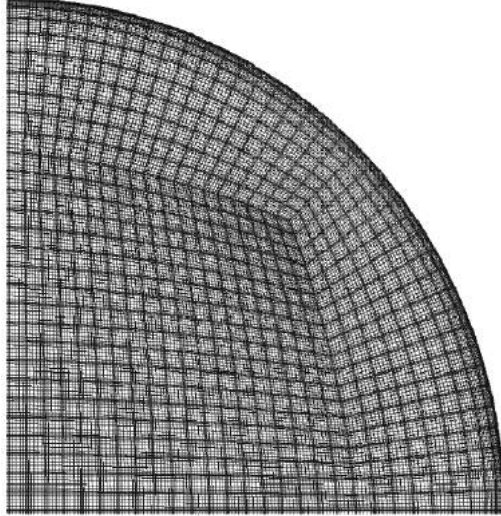


Figure 7: Quarter section of the computational mesh corresponding to case 2 from Table 1, at $Re_\tau = 550$. Spectral element boundaries are shown with thicker lines, whereas thin ones represent the individual GLL points. Polynomial order $N = 7$ was considered in this particular setup.

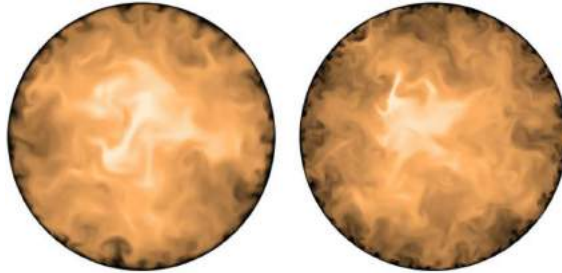


Figure 8: Instantaneous streamwise velocity U normalized with pipe bulk velocity U_b corresponding to cases (left) 2 and (right) 3 from Table 1, at $Re_\tau = 550$ and 1,000 respectively. Note that the velocity varies from 0 (black) to 1.3 (white).

9. The communication, computation and total time for 20 timesteps, excluding I/O, are plotted as a function of the number of nodes. The corresponding number of cores (and MPI ranks) is found by multiplying the number of nodes by 32. The scaling has been performed for both coarse grid solvers XXT and AMG. In general, the difference between XXT and AMG is small but can lead up to a 10% reduction in total time in favor of AMG. We define the strong scaling limit as the point where computation and communication times are equal. On Beskow, it is reached for about 20000 – 50000 gridpoints per core.

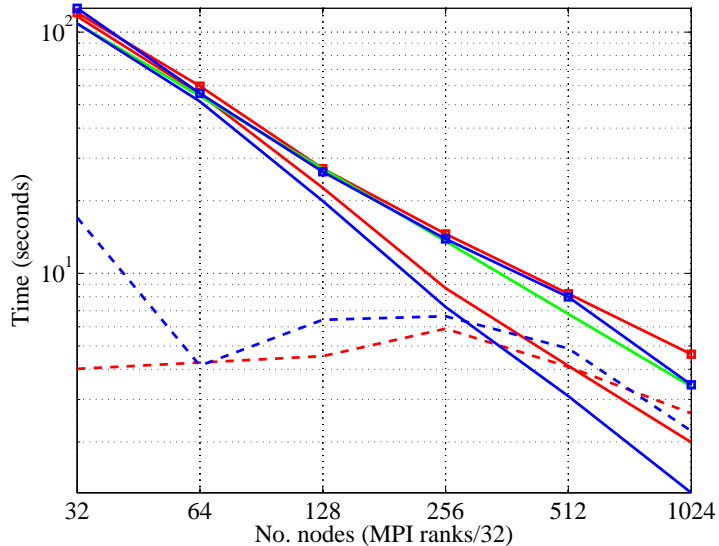


Figure 9: Strong scaling of the turbulent flow in a pipe for $Re_\tau = 550$ on Beskow. AMG (blue), XXT (red), communication (dashed), computation (solid), total time (\square), computational linear scaling (green).

6 Incompressible flow around a NACA4412 wing section

We will consider a total of 5 test cases based on the incompressible turbulent flow around a NACA4412 wing section, at Reynolds numbers Re_c ranging from 50,000 to 1,000,000, all of them with 5° angle of attack. The airfoil geometry includes a sharp trailing edge, obtained by modifying the corresponding coefficient in the NACA airfoil equation. Initially a RANS simulation is performed by means of the code EDGE developed at FOI Eliasson (2002), which uses the explicit algebraic Reynolds stress model (EARSM) by Wallin and Johansson Wallin & Johansson (2000). The RANS domain extends up to $200c$ in every direction, and this RANS solution is used to extract an accurate velocity distribution in the near field corresponding to the time-averaged flow at a given angle of attack. This distribution is then imposed as Dirichlet boundary conditions on the DNS domain. We considered a C-mesh topology of radius c centered at the leading edge of the airfoil, with total domain lengths of $6.2c$ in the horizontal (x), $2c$ in the vertical (y) and $0.1c$ in the spanwise (z) directions, see Figure 10. Periodicity is imposed in the spanwise direction, and the natural stress-free boundary condition at the outlet. The computational mesh was optimized based on distributions of the Kolmogorov scale $\eta = (\nu^3/\varepsilon)^{1/4}$, where ν is the kinematic viscosity and ε is the local isotropic dissipation. The design criterion was $h \equiv (\Delta x \cdot \Delta y \cdot \Delta z)^{1/3} < 4 - 5\eta$ everywhere in the domain, which ensures that the mesh is fine enough to capture the smallest turbulent scales. Note that the flow is tripped at $x/c = 0.1$ on both suction and pressure sides, using the volume forcing approach by Schlatter and Örlü Schlatter & Örlü (2012). The initial condition is the RANS solution, and the flow is initially run for around three flow-over times with polynomial order $N = 5$.

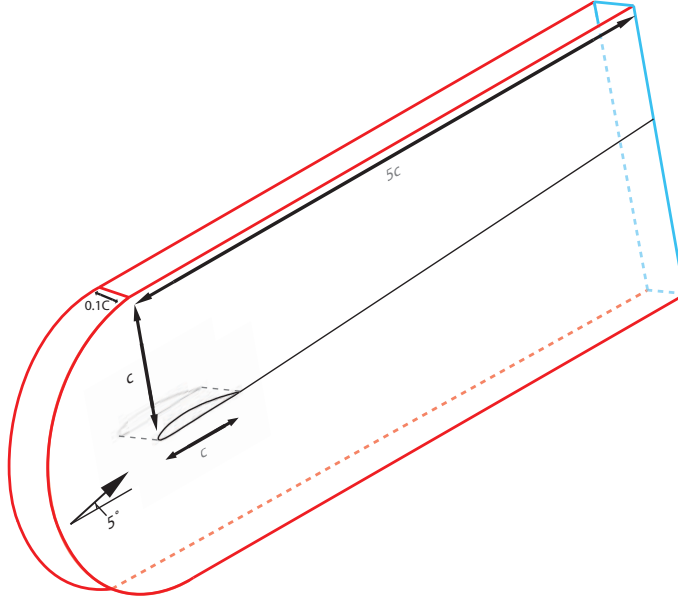


Figure 10: Schematic three-dimensional layout of the set up for direct numerical simulation. The chord length is denoted as c . The domain extends to up $5c$ downstream, and $1c$ upstream, top and bottom from the leading edge. The red lines mark the boundaries where the Dirichlet condition was used. The blue line indicates the boundaries with the stress-free condition. The incoming flow has an angle of attack of 5° , and the Cartesian coordinate system is aligned with the chord.

After this point the polynomial order is progressively increased up to the final value of $N = 11$. A full description of the setup is given by Vinuesa *et al.* Vinuesa *et al.* (2015) for a case with $Re_c = 400,000$, where 1.85 million spectral elements with $N = 11$ were used, which leads to a total of 3.2 billion grid points. An instantaneous visualization of the flow field, together with the spectral element mesh from the $Re_c = 400,000$ case, are shown in Figure 12. The smoothness of even the smallest vortical structures shows that the setup is appropriate to simulate all the relevant flow features.

The wing cases under consideration for the ExaFLOW project are summarized in Table 2, including a 2D simulation at low Reynolds number, and both direct numerical and large-eddy simulation cases, in order to cover a wide range of scaling effects. Note that the LES is based on the approach proposed by Schlatter *et al.* Schlatter *et al.* (2004), where a dissipative relaxation term is added to the right-hand side of the Navier–Stokes equations. This term provides all the necessary drain of energy out of the coarsely discretized system, and previous validations in zero pressure gradient boundary layers Eitel-Amor *et al.* (2014) show excellent agreement between DNS and LES.

Scaling tests performed at the Cray-XC40 computer “Beskow” at PDC (KTH) are shown in Figure 11, for case 3 from Table 2 (left) and for a configuration similar to case 2 with a total of 120 million grid points (right). In order to establish a good measure of scaling, we report the time required to perform one GMRES (generalized minimal residual method) iteration for the pressure solve. Doing so, we can characterize code performance by isolating it from other factors contributing to the total time per time-step, such as I/O

Case #	Simulation	Re_c	# grid points
1	2D	50,000	88×10^3
2	DNS	100,000	82×10^6
3	DNS	400,000	3.2×10^9
4	LES	400,000	530×10^6
5	LES	1,000,000	6.0×10^9

Table 2: Summary of wing cases for ExaFLOW project

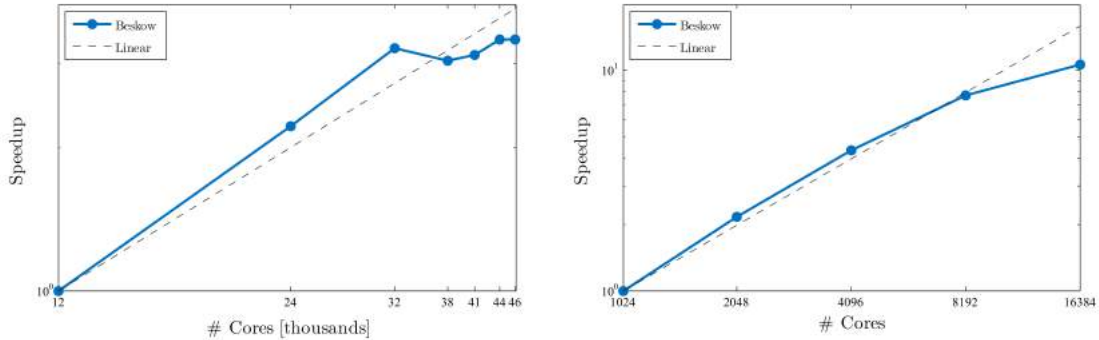


Figure 11: Strong scaling results performed on the “Beskow” system at PDC (KTH). Test cases with a total of (left) 3.2 billion and (right) 120 million grid points.

operations, different tolerances etc. Note that in case 3 the best performance is achieved when running on 32,768 cores (with around 100,000 grid points per core), and in the modified case 2 the best scaling is observed on 4,096 cores, with a total of 30,000 grid points per core.

References

- Alferez, N., Mary, I. & Lamballais, E. (2013), ‘Study of stall development around an airfoil by means of high fidelity large eddy simulation’, *Flow Turbulence Combust* **91**(3), 623–641.
URL: <http://dx.doi.org/10.1007/s10494-013-9483-7>
- Eitel-Amor, G., Örlü, R. & Schlatter, P. (2014), ‘Simulation and validation of a spatially evolving turbulent boundary layer up to $re\theta=8300$ ’, *International Journal of Heat and Fluid Flow* **47**, 57–69.
- El Khoury, G. K., Schlatter, P., Noorani, A., Fischer, P. F., Brethouwer, G. & Johansson, A. V. (2013), ‘Direct numerical simulation of turbulent pipe flow at moderately high reynolds numbers’, *Flow, turbulence and combustion* **91**(3), 475–495.
- Eliasson, P. (2002), Edge, a navier-stokes solver for unstructured grids., *in* D. Kroner & R. Herbin, eds, ‘Proceedings to Finite Volumes for Complex Applications III.’, Hemre Penton Science London, pp. 527–534.

- Fischer, P. F. (1997), ‘An Overlapping Schwarz Method for Spectral Element Solution of the Incompressible Navier Stokes Equations’, *Journal of Computational Physics* **133**, 84–101.
- Fischer, P. F., Lottes, J. W. & Kerkemeier, S. G. (2008), ‘nek5000 Web page’. <http://nek5000.mcs.anl.gov>.
- Fischer, P. F. & Patera, A. T. (1994), ‘Parallel simulation of viscous incompressible flows’, *Annual Review of Fluid Mechanics* **26**, 483–527.
- Fischer, P., Lottes, J., Pointer, D. & Siegel, A. (2008), ‘Petascale algorithms for reactor hydrodynamics’, *Journal of Physics Conference Series* **125**(1), 012076.
- Jeong, J. & Hussain, F. (1995), ‘On the identification of a vortex’, *Journal of Fluid Mechanics* **285**, 69–94.
- Karagozian, A. R. (2010), ‘Transverse jets and their control’, *Progress in Energy and Combustion Science* **36**, 531–553.
- Mahesh, K. (2013), ‘The interaction of jets with crossflow’, *Annual Review of Fluid Mechanics* **45**, 379–407.
- Rodríguez, I., Lehmkuhl, O., Borrell, R. & Oliva, A. (2013), ‘Direct numerical simulation of a {NACA0012} in full stall’, *International Journal of Heat and Fluid Flow* **43**, 194 – 203. 7th International Symposium on Turbulence Heat & Mass Transfer (THMT-7), Palermo Conference on Modelling Fluid Flow (CMFF12).
URL: <http://www.sciencedirect.com/science/article/pii/S0142727X13000891>
- Schlatter, P. & Örlü, R. (2012), ‘Turbulent boundary layers at moderate reynolds numbers: inflow length and tripping effects’, *Journal of Fluid Mechanics* **710**, 5–34.
- Schlatter, P., Stolz, S. & Kleiser, L. (2004), ‘LES of transitional flows using the approximate deconvolution model’, *International journal of heat and fluid flow* **25**(3), 549–558.
- Shan, H., Jiang, L. & Liu, C. (2005), ‘Direct numerical simulation of flow separation around a {NACA} 0012 airfoil’, *Computers & Fluids* **34**(9), 1096 – 1114.
URL: <http://www.sciencedirect.com/science/article/pii/S0045793004001203>
- Vinuesa, R., Hosseini, S. M., Hanifi, A., Henningson, D. S. & Schlatter, P. (2015), ‘Direct numerical simulation of the flow around a wing section using high-order parallel spectral methods’, *Int. Symp. Turbulence & Shear Flow Phenomena (TSFP-9)* **30**.
- Wallin, S. & Johansson, A. V. (2000), ‘An explicit algebraic reynolds stress model for incompressible and compressible turbulent flows’, *Journal of Fluid Mechanics* **403**, 89–132.

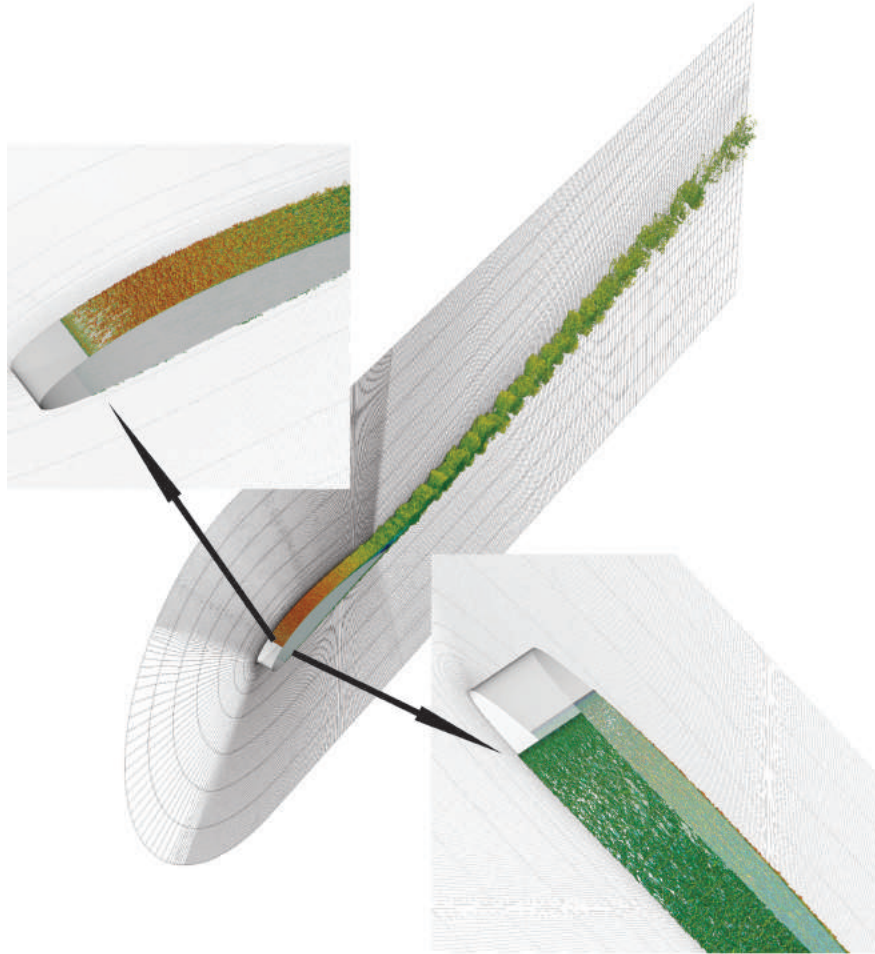


Figure 12: Instantaneous vortical structures visualized with the λ_2 criterion Jeong & Hussain (1995), colored with chordwise velocity, ranging from -0.1 (dark blue) to 1.5 (red). The flow is tripped at 10% chord on both sides. The angle of attack is 5° and the chord Reynolds number is $Re_c = 400,000$. The spectral element mesh is also shown, but not the individual grid points within elements.

ExaFLOW use case for SBLI: numerical simulation of the compressible flow over a NACA-4412 airfoil at incidence

Nico De Tullio¹, Neil D. Sandham¹,
Michael R. Bareford², Christian T. Jacobs¹

¹Aerodynamics and Flight Mechanics Group
University of Southampton
Southampton SO17 1BJ, UK

²Edinburgh Parallel Computing Centre
University of Edinburgh
Edinburgh EH9 3FD, UK

1 Introduction

This use case considers the compressible, subsonic flow over a NACA-4412 airfoil at 5° incidence, for a freestream Mach number $M_\infty = 0.4$ and Reynolds number based on the airfoil chord of $Re_c = 50000$. The airfoil geometry, which includes a sharp (zero thickness) trailing edge, was obtained by modifying the last coefficient in the 4-digit NACA airfoil equation (see equation 6.2 in Abbot and von Doenhoff [1959]) from -0.1015 to -0.1036 . This modification leads to a sharp trailing edge, with minimal changes to the overall airfoil geometry. The two-dimensional (2D) base flow over the NACA-4412 airfoil was calculated using the 2D compressible Navier-Stokes equations. The flow is unsteady and includes vortex shedding from a laminar separation bubble that forms on the suction side of the airfoil, as can be seen in Figure 1. The interaction between these vortices and the trailing edge of the airfoil causes the scattering of acoustic waves and leads to the acoustic field shown in Figure 2 through contours of the dilatation rate $\nabla \cdot \mathbf{u}$. This use case is suitable for examining the performance of the algorithmic improvements for exascale computation, because of the large Reynolds number encountered resulting in extremely turbulent dynamics. This demands very high numbers of grid points and small time-step sizes in order to resolve the dynamics with sufficient accuracy and stability, and therefore requires exascale-capable software and hardware to run the simulation in parallel within a feasible amount of time.

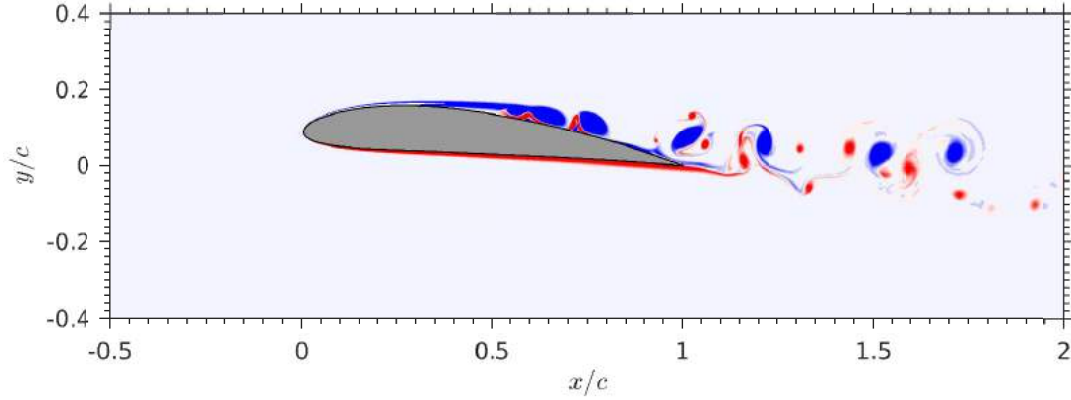


Figure 1: Instantaneous contours of spanwise vorticity ω_z . 50 contour levels plotted over a range $[-50, 50]$. Blue for negative and red for positive.

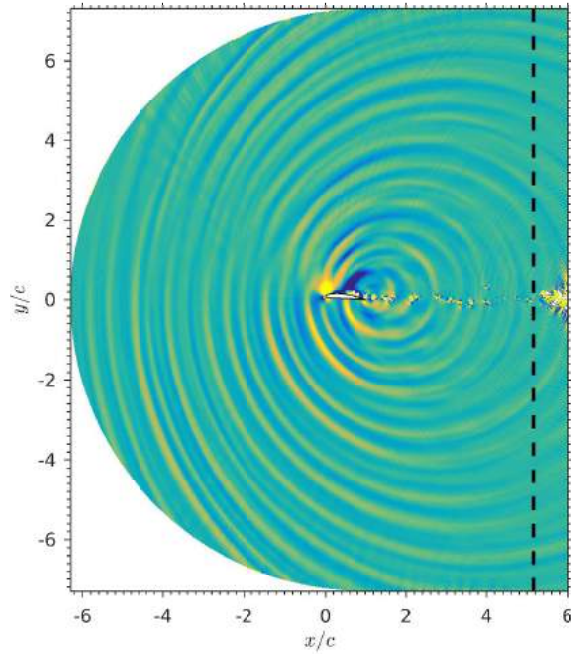


Figure 2: Instantaneous contours of dilatation rate. 50 contour levels plotted over a range $[-0.1, 0.1]$. Blue for negative and yellow for positive. The dashed black line indicates the start of the zonal characteristic boundary condition.

In the numerical simulations described here, the computational domain is extruded in the spanwise direction and the three-dimensional (3D) Navier-Stokes equations are advanced in time starting from a 2D solution. The flow is assumed to be periodic in the spanwise direction. Since no external 3D disturbances are added to the simulations, the numerical solution should remain 2D.

2 Overview of numerical algorithm

The compressible Navier-Stokes equations are numerically solved using the SBLI code, which is a finite difference compressible Navier-Stokes solver developed at the University of Southampton. The spatial discretisation of the equations uses a standard fourth-order central difference scheme at internal points and a stable boundary treatment proposed by Carpenter et al. [1999] close to boundaries, giving overall fourth-order accuracy. Time integration is based on a third-order compact Runge-Kutta method [Wray, 1990]. The code employs an entropy splitting approach developed by Sandham and co-workers [Sandham et al., 2002], whereby the inviscid flux derivatives are split into conservative and non-conservative parts. The entropy splitting scheme, together with a Laplacian formulation of the heat transfer and viscous dissipation terms in the momentum and energy equations (which prevents the odd-even decoupling typical of central differences, see Sandham et al. [2002]), helps improve the stability of the low dissipative spatial discretisation used. The code has multi-block capabilities and is made parallel (both intra- and inter-block) using the message passing interface (MPI) library. The code has been validated extensively (see for example De Tullio and Sandham [2010], De Tullio [2013], De Tullio et al. [2013]).

3 Computational domain and grid arrangement

The computational domain is composed of three blocks, as can be seen in Figure 3(a). Block 2 is a C-type structured grid fitted around the airfoil surface; it interfaces with the structured blocks 1 and 3, which resolve the wake of the airfoil. Since block 1 and block 3 both contain the wake line, the wake line solution at each time step is obtained by averaging between the solutions obtained in the two blocks. This is necessary because flow asymmetries near the airfoil trailing edge and/or small differences in initial conditions will cause the wake line solutions in the two blocks to diverge. For the current numerical simulations the computational domain dimensions are $W = 5.0c$ and $R = 7.3c$ (see Figure 3(a)), where c is the chord length. The total domain length is $12.3c$ and the total height is $14.6c$.

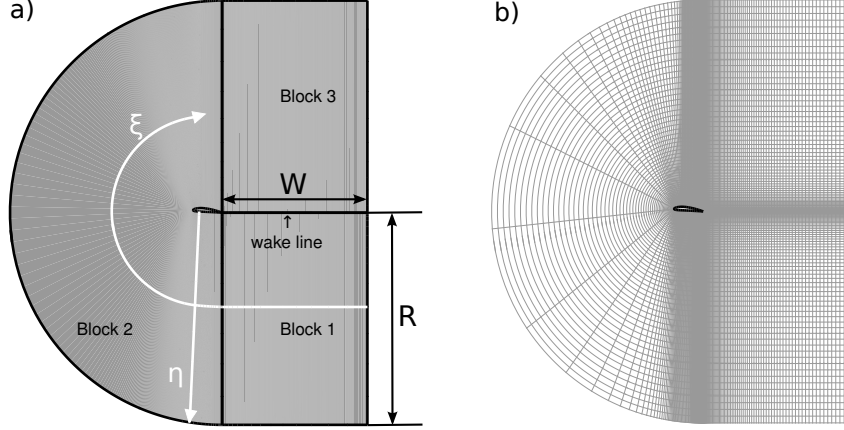


Figure 3: Computational domain arrangement. (a) multi-block domain set up, (b) computational grid, showing only one in every 10 grid points.

The numerical simulations will be carried out using characteristic conditions at all the computational domain boundaries, in order to minimize wave reflections. In particular, a zonal characteristic boundary condition [Sandberg and Sandham, 2006] is applied over a distance $L_{zonal} \approx 0.85c$ near the outflow boundary of blocks 1 and 3, using 61 grid points. A standard characteristic condition [Thomson, 1987, 1990] is applied at the rest of the boundaries, where, in addition, the freestream solution is imposed at each time step. The airfoil is modelled using a no-slip, isothermal boundary condition, with the wall temperature equal to the freestream temperature.

	x	y	$\Delta\xi$	$\Delta\eta$
Stagnation point	0.004	0.086	1×10^{-3}	2.5×10^{-4}
Trailing edge	1.0	0.0	5.0×10^{-4}	2.5×10^{-4}
Exit boundary	6.0	0.0	1.5×10^{-2}	3.2×10^{-4}
Exit/Free stream boundary	6.0	7.3	1.5×10^{-2}	2.3×10^{-2}

Table 1: Grid resolution at key points in the domain.

Block	1	2	3
N_ξ	801	1799	801
N_η	692	692	692

Table 2: Number of grid points per block.

A representation of the computational grid employed in the current numerical simulations is shown in Figure 3(b), where only one in every ten grid points are plotted, while grid resolutions at key points in the domain, for the ξ and η directions, are given in Table 1. The number of grid points employed per block for a 2D slice of the grid is given in Table 2. The grid was designed to resolve all the flow features around the airfoil and the

far field acoustic waves generated by the flow structures, for the current Reynolds and Mach numbers. This 2D grid is extruded in the z direction (wing span) using a constant grid spacing of $\Delta z = 0.002$. The number of grid points to be used along the span N_z is a user specified parameter that can be used to modify the size of the numerical simulation. Since we impose Δz to be a constant, changing N_z means changing the spanwise extension of the computational domain.

4 Input data

The input data needed to start a simulation are: an input file (`Input.in`) with flow and numerical parameters, a binary grid file (`Airfoil_3D.bin`) that contains the computational grid coordinates and additional information regarding the multi-block domain layout, boundary conditions per block, processor distribution per block, etc. and one restart file per block (`Qfile_r1`, `Qfile_r2` and `Qfile_r3`) with flowfield and boundary data.

An excerpt of the file `Input.in` is shown below:

```
#Mach, Reynolds, Prandtl, Schmidt, Gamma, Omega
0.4, 50000, 0.72, 1.0, 1.4, 0.76
#Sutherland: temp. const. (K), ref. temp. (K)
110.4, 273.15
#CFL, dt, use CFL to calc dt ?
2.0, 0.00010, .f.
#Time step number, plot3d output step, max time
1000,1000,5000.0
#Input file, Binary input grid?, Fortran 77 input grid?
'Airfoil_3D.bin',.t.,.f.
#Restart?, Restart input file directory
.t.,'. '
#Output?, Output dir., Qfile output step (-1: at the end)
.f.,'RESULTS/',-1
#Num. of monitor points, then i,j,k, & block num. for each
5 1371 10 1 2 1524 10 1 2 1 10 1 3 191 10 1 3 191 10 4 3
```

It can be seen that the simulation is set up to run 1000 time steps. The values of the conservative variables (ρ , ρu , ρv , ρw and ρE) at five monitor points (see line 8) will be recorded every 100 time steps and saved in five `monitor_point.i` (i from 1 to 5) files at the end of the simulation. No additional output will be saved, unless the user modifies the first element in line 7 of the file `Input.in` to read `.t..` The output time step period can be specified in line 4 for single precision `plot3d` files and in line 7 for double precision `Qfile` files. The `Input.in` file is located in the folder `../Test_Case/Execute/` from which the code executable `pdns3d.x` should be run. The executable can be generated using the `Makefile` in `../Test_Case/Code/`.

The file `Airfoil_3D.bin` is generated by the `BuildGridBinary.f` Fortran routine, which needs as inputs the number of grid points in the spanwise direction and the number of processors in all the three directions per block. The `BuildGridBinary.f` routine

accesses the above information through the input file `Grinput.in`. It is important to note that block 2 contains about 2.25 times the number of grid points in blocks 1 and 3, meaning that block 2 should have about 2.25 times the number of processors assigned to block 1 and block 3, for load balancing purposes (blocks are not allowed to share processors). In addition, the zonal characteristic boundary condition applied near the outflow of blocks 1 and 3 (across 61 grid points) cannot cross processor boundaries, hence the maximum number of processors in the ξ direction for this two blocks is 12.

Files `Qfile_r1`, `Qfile_r2` and `Qfile_r3` are generated by the Fortran routine `Extrude_2DField.f`, which also uses the `Grinput.in` file for input. The Fortran routines `BuildGridBinary.f` and `Extrude_2DField.f` are located in `../Test_Case/Grid/`, together with all the files needed for the generation of the computational grid. Once generated, the binary files `Airfoil_3D.bin`, `Qfile_r1`, `Qfile_r2` and `Qfile_r3` should be moved to the folder `../Test_Case/Execute/`.

5 Standard output

The set up of the current simulation is such that the SBLI code will only give five `monitor_point.i` (i from 1 to 5) files as output. These files will be generated in `../Test_Case/Execute/` at the end of the simulation; they contain the values of the conservative variables every 100 time steps at five different points in the domain. As an example, the contents of the file `monitor_point.1` are shown in Table 3. Note that point number 5 has the same x - and y -coordinates as point 4, but different z -coordinate. However, since the flow should remain 2D, these two files should be identical. The monitor point files obtained for a case with 5 grid points in the spanwise direction can be found in the folder `../Test_Case/Execute/Monitoring_Points/`

6 Preliminary scaling results

A set of scaling runs was performed with the latest version (v4.2.0) of the SBLI code. Table 4 gives the sequence of node counts for each scaling run. P is the number of processors, $P_{1,3}$ is the number of processors used for blocks 1 and 3 (i.e., $P_1 = P_3$) and $(P_\xi)_2$ is the number of processors in the ξ dimension used for block 2. Table 4 also shows how the number of processors (24 per node) are divided amongst the three blocks, such that $P_2/P_{1,3} \approx 2.25$ (note, blocks 1 and 3 are treated identically). Furthermore, within each block, the processor count is broken down by dimension such that $(P_\xi)_{1,3} \leq 12$.

# nodes	P	$P_{1,3}$	$(P_\xi \times P_\eta \times P_z)_{1,3}$	P_2	$(P_\xi \times P_\eta \times P_z)_2$
4	96	22	$11 \times 2 \times 1$	52	$26 \times 2 \times 1$
8	192	45	$9 \times 5 \times 1$	102	$17 \times 6 \times 1$
16	384	90	$9 \times 5 \times 2$	204	$17 \times 6 \times 2$
32	768	180	$9 \times 5 \times 4$	408	$17 \times 6 \times 4$
64	1536	360	$9 \times 5 \times 9$	40	$1 \times 48 \times 1$

Table 4: Processor Decomposition.

Step	time	ρ	ρu	ρv	ρw	ρE
1000000	0.10000000E+03	0.89329195E+00	0.22677297E+00	-0.64542249E-01	00000000E+00	0.99486173E+01
1000100	0.10001000E+03	0.89123269E+00	0.21704640E+00	-0.50826718E-01	00000000E+00	0.99261284E+01
1000200	0.10002000E+03	0.88944252E+00	0.22974307E+00	-0.33023594E-01	00000000E+00	0.99169495E+01
1000300	0.10003000E+03	0.88862728E+00	0.27104728E+00	-0.22318973E-01	00000000E+00	0.99301942E+01
1000400	0.10004000E+03	0.88904274E+00	0.34514868E+00	-0.19861198E-01	00000000E+00	0.99662313E+01
1000500	0.10005000E+03	0.89085059E+00	0.44563483E+00	-0.20426127E-01	00000000E+00	0.10025899E+02
1000600	0.10006000E+03	0.89368558E+00	0.51468416E+00	-0.35578044E-01	00000000E+00	0.10085324E+02
1000700	0.10007000E+03	0.89643240E+00	0.48810331E+00	-0.70115296E-01	00000000E+00	0.10107626E+02
1000800	0.10008000E+03	0.89978262E+00	0.39417874E+00	-0.10434086E+00	00000000E+00	0.10120412E+02
1000900	0.10009000E+03	0.90413431E+00	0.26230020E+00	-0.12572211E+00	00000000E+00	0.10142470E+02
1001000	0.10010000E+03	0.90821967E+00	0.97483446E-01	-0.13070930E+00	00000000E+00	0.10161082E+02

Table 3: Contents of the `monitor_point.1` file.

The number of time steps executed varies with granularity; it is set such that the runtime is approximately one hour when running on four nodes. The test runs for the first three granularities ($\sqrt[3]{G} = 16, 24, 32$) execute 8000 iterations, 5000 iterations are used for $\sqrt[3]{G} = 48$ and 8000 for $\sqrt[3]{G} = 64$. The runtimes are shown in Table 5 and plotted in Figure 4, which shows good scaling of the SBLI code for this problem.

# nodes	$\sqrt[3]{G}$				
	16	24	32	48	64
4	4019 (2)	3997 (2)	4028 (2)	4326 (5)	4769 (11)
8	1862 (2)	12824 (2)	2466 (3)	3235 (9)	4159 (21)
16	840 (2)	846 (2)	1601 (5)	3596 (18)	4709 (43)
32	352 (2)	751 (5)	1603 (11)	3815 (36)	5095 (86)
64	455 (3)	594 (9)	1701 (21)	3879 (72)	5104 (172)

Table 5: NACA4412 runtimes in seconds (with N_z , the number of grid points in the z dimension, in brackets) for the scaling runs involving granularities of $\sqrt[3]{G} \in 16, 24, 32, 48, 64$. G is the number of grid points per processor.

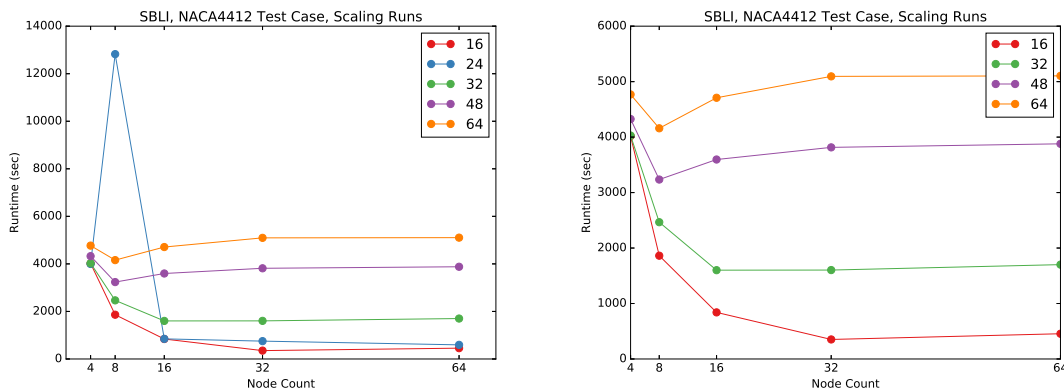


Figure 4: Runtimes for scaling runs at five different granularities. An un-usually high runtime is produced for $\sqrt[3]{G} = 24$ over eight nodes - this result is removed from the right plot.

7 Preliminary power monitoring results

In addition to scalability, codes must be economical in their power usage as progress is made towards exascale computation. For this reason, the SBLI v4.2.0 source code has been instrumented such that the energy usage and power consumption are measured at various points within each time step of the NACA4412 simulation. Several calls to the monitoring library, `pat_mpi.lib` [Bareford, 2015a] are placed inside the main application loop of the `pdns3d` program (see the `main_3d.f` source file). The `pat_mpi.lib` library accesses the hardware counters via the CrayPAT API [Cray Inc., 2012] and has the advantage that controlling which counters are monitored does not require programmatic

changes, either to the monitoring library or to the code under investigation. Instead, the monitored counters are specified by setting environment variables in the submission script, see slides 23-29 of Bareford [2015b].

The NACA4412 test case was run six times over four compute nodes (ninety six processors) on the ARCHER Cray XC30 platform [EPCC, 2015]. Each run involved one thousand time steps and took around fifteen minutes to execute. The SBLI code was compiled with the Cray Programming Environment v5.2.56 available on ARCHER as of 15 January 2015. All readings are taken on a per node basis and then either averaged or summed to provide an overall measurement. For example, power readings are averaged, whereas energy readings are added together.

In general, the point-in-time power histograms (Figure 5) are asymmetric about the maximum with more readings below the peak value than above. The minimum reading of ≈ 273 W, present in all the histograms, is the first reading from the first time step of the simulation. There is a noticeable increase in the power readings over the first 2-3 minutes, see Figure 6 – this explains the asymmetry of the histograms.

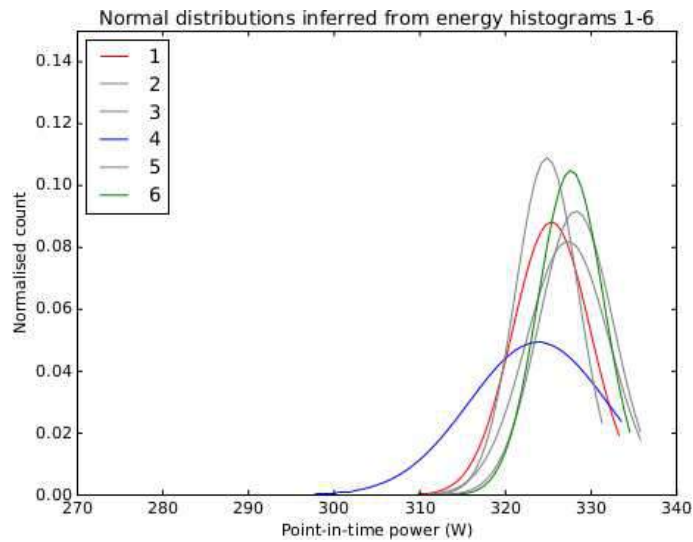


Figure 5: Normal distributions inferred from the point-in-time power histograms generated by all six runs.

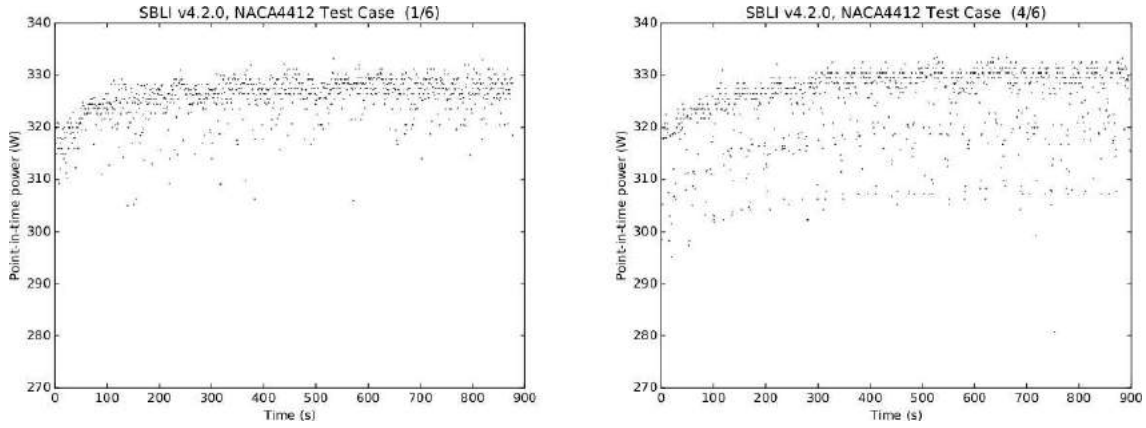


Figure 6: The point-in-time power readings for the first and fourth simulation runs.

The total DRAM energy usage was 6.025 ± 0.082 MJ over 881 ± 8.9 s. The DRAM energy readings are highest at the start of the run and then, during the first half of the simulation, fall (by roughly 8%) to a steady average (see Figure 7).

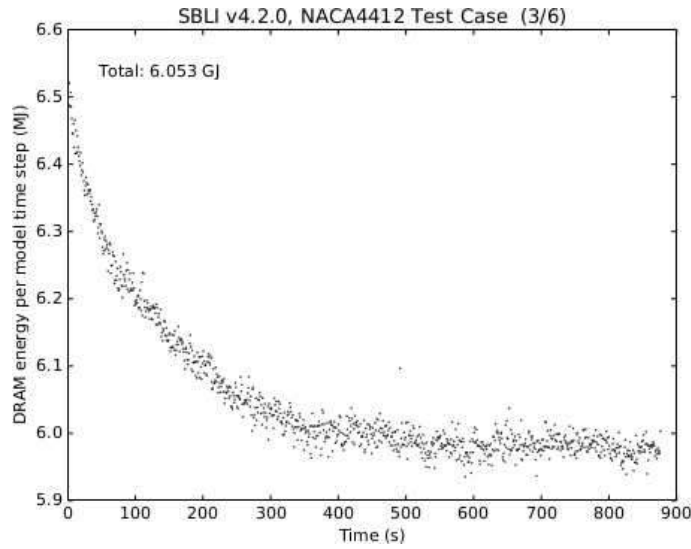


Figure 7: DRAM energy used per time step throughout run 3 (of 6).

These baseline power and energy readings can be compared throughout the ExaFLOW project in order to evaluate the algorithmic improvements made in WP1 and their implementation in WP2.

References

I.H. Abbot and A.E. von Doenhoff. *Theory of wing sections*. Dover Publications, 2nd edition, 1959.

- M. R. Bareford. The pat mpi library. GitHub repository: https://github.com/cresta-eu/pat_mpi.lib. Online, 2015a.
- M. R. Bareford. Monitoring the cray xc30 power management hardware counters: https://cug.org/proceedings/cug2015_proceedings/includes/files/pap125-file2.pdf. Online, 2015b.
- M. H. Carpenter, J. Nordstrom, and D. Gottlieb. A stable and conservative interface treatment of arbitrary spatial accuracy. *Journal of Computational Physics*, 148:341–365, 1999.
- Cray Inc. Using Cray Performance Measurement and Analysis Tools: <http://docs.cray.com/books/S-2376-60/>. Online, 2012.
- N. De Tullio. *Receptivity and transition to turbulence of supersonic boundary layers with surface roughness*. PhD thesis, School of Engineering Sciences, University of Southampton, 2013.
- N. De Tullio and N. D. Sandham. Direct numerical simulation of breakdown to turbulence in a Mach 6 boundary layer over a porous surface. *Physics of Fluids*, 22(094105), 2010.
- N. De Tullio, P. Paredes, N. D. Sandham, and V. Theofilis. Laminar-turbulent transition induced by a discrete roughness element in a supersonic boundary layer. *J. Fluid Mech.*, 735:613–646, 2013.
- EPCC. Archer user guide: <http://www.archer.ac.uk/documentation/user-guide/>. Online, 2015.
- R.D. Sandberg and N.D. Sandham. Nonreflecting zonal characteristic boundary condition for direct numerical simulation of aerodynamic sound. *AIAA J.*, 44(2):402–405, 2006.
- N. D. Sandham, Q. Li, and H. C. Yee. Entropy splitting for high-order numerical simulation of compressible turbulence. *Journal of Computational Physics*, 178:307–322, 2002.
- K. W. Thomson. Time dependent boundary conditions for hyperbolic systems. *Journal of Computational Physics*, 68:1–24, 1987.
- K. W. Thomson. Time dependent boundary conditions for hyperbolic systems, II. *Journal of Computational Physics*, 89:439–461, 1990.
- A. A. Wray. Minimal storage time advancement schemes for spectral methods. Rept. M.S. 202 A-1., NASA Ames Research Centre, 1990.

ExaFLOW use case: Numerical simulation of the rear wake of a sporty vehicle

C. J. Falconi D.¹, D. Lautenschlager²

¹*Automotive Simulation Center Stuttgart e. V.
Nobelstraße 15, 70569 Stuttgart, Germany*

²*Adam Opel AG
Friedrich-Lutzmann-Ring, 65423 Rüsselsheim, Germany*

1. Introduction

The test case under consideration is the airflow around the vehicle OPEL Astra GTC. This vehicle was designed by the automobile manufacturer Adam Opel AG. Additionally to windtunnel testing this vehicle was aerodynamically developed by using Computational Fluid Mechanics (CFD) applying the Reynolds-averaged Navier-Stokes equations (RANS) for the full detail vehicle model. For a more detailed understanding of the behavior of turbulent structures Detached Eddy Simulations (DES) were used for simplified submodel domains. The Reynolds number is equal $Re=6.3 \times 10^6$ using the wheel base ($L=2.695\text{m}$) as the characteristic length and the INLET velocity (140km/h) as reference velocity.

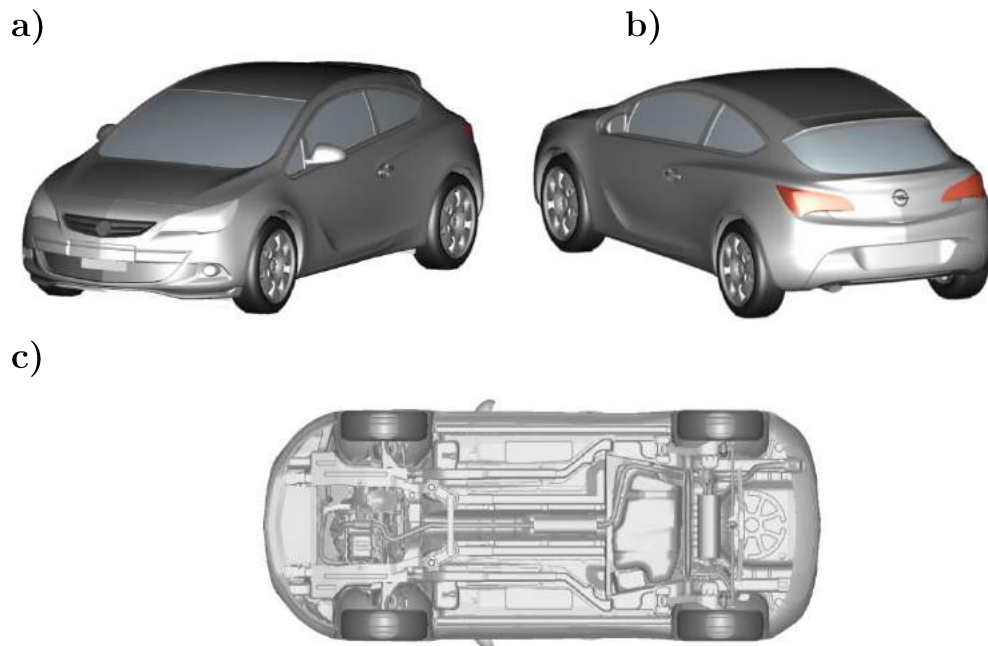


Figure 1: Geometry of the Opel Astra GTC. a) Front top view, b) Rear top view, c) Bottom view.

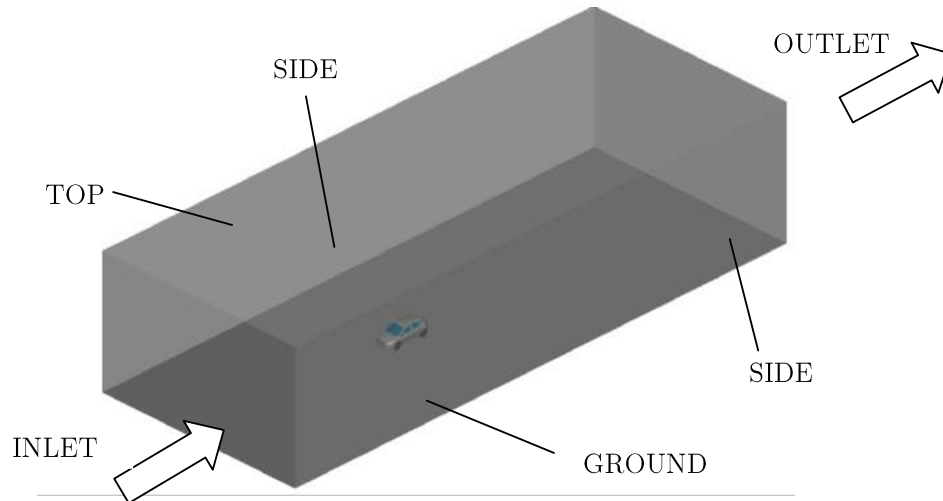


Figure 2: Computational domain of the completely vehicle model in the wind tunnel.

The respective simulations were initially performed with the commercial software ANSYS Fluent version 6.122 during the development process of the vehicle. In order to provide the first requirements and description of the automotive use case in the frame of the Exaflow project the simulation results were updated by the use of ANSYS Fluent 14.0.

After describing the geometry of the vehicle in section 2, the complete vehicle model will be described in section 3 followed by the description of the so called submodel in section 4. In the last section the need of exascale capabilities for the use case is specified.

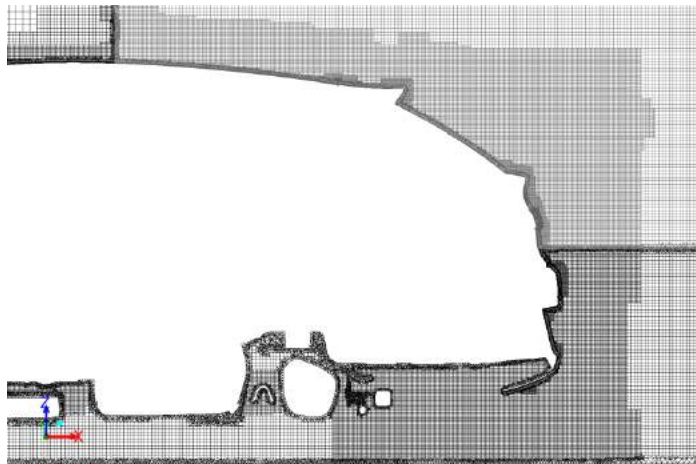


Figure 3: X-Z plane of the numerical mesh used for the completely vehicle model at the middle of the vehicle

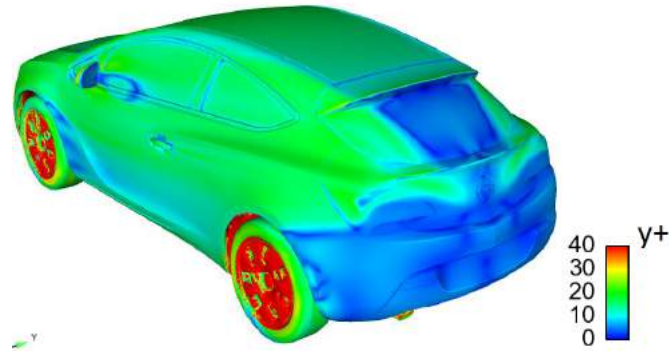


Figure 4: Distribution of the non-dimensional wall distance y^+ .

2. Vehicle geometry

The Opel Astra GTC is a 3-door sporty looking vehicle; the vehicle is 4.468m long, 1.991m wide and 1.449 m height (see Fig 1a, 1b, 1c). In order to ensure a successful mesh generation process a high quality CAD model is required. The engine compartment and the underbody are modeled in full detail in order to capture all relevant aerodynamic effects.

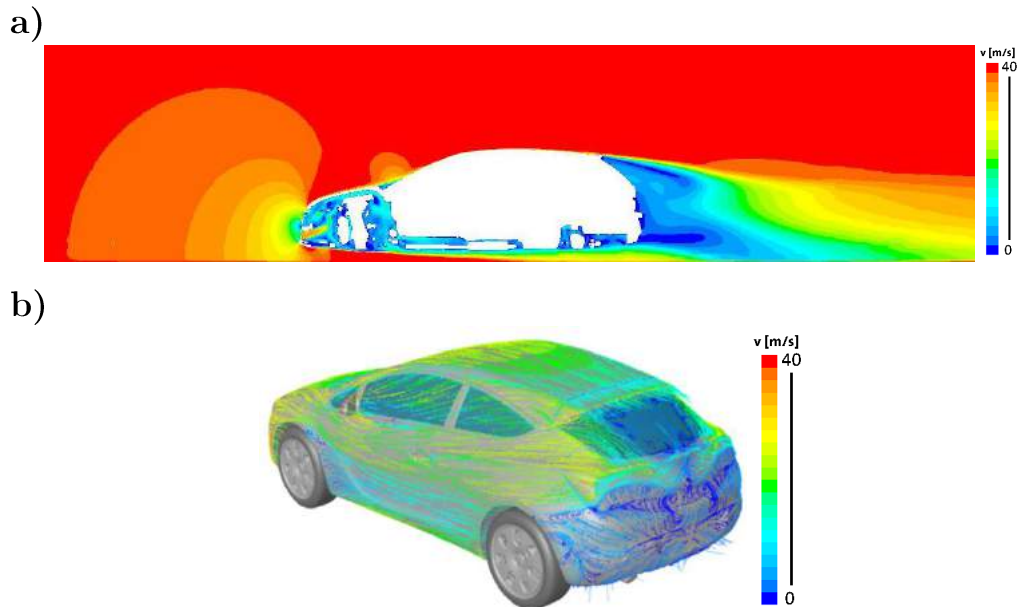


Figure 5: Simulation results (*RANS*) of the complete vehicle model. a) 2D contour of the velocity magnitude at the middle of the vehicle. b) Streamlines colored by the velocity magnitude.

3. Complete simulation model

The complete simulation model consists of the entire vehicle geometry described in section 2 and the virtual wind tunnel as depicted in Figure 2. The wind tunnel is 51m long, 20m wide and 12m high.

3.1 Numerical method

Simulations were performed using the Reynolds-averaged Navier–Stokes equations (RANS). The turbulence effects were modelled by the realizable $k-\varepsilon$ model. The numerical mesh on the surface of the vehicle was generated with the commercial mesh generator ANSA. The typical length of the elements on the external surface is between 1-6mm, while surfaces near the underbody region were meshed with a length between 2-12mm. The total number of elements of the completely 2D surface mesh is 3.4 million.

Based on the surface mesh, a 3D volume mesh was created with the commercial mesh generator TGrid. A non-conformal Hexcore mesh (Hexaeder and Tetraeder) was generated with 7 prism layers on the exterior surface of the vehicle and the wind tunnel ground. Additionally the mesh is gradually refined near the vehicle surface and the wake area as depicted in Figure 3 resulting in a total number of 95 million cells in the entire computational domain.

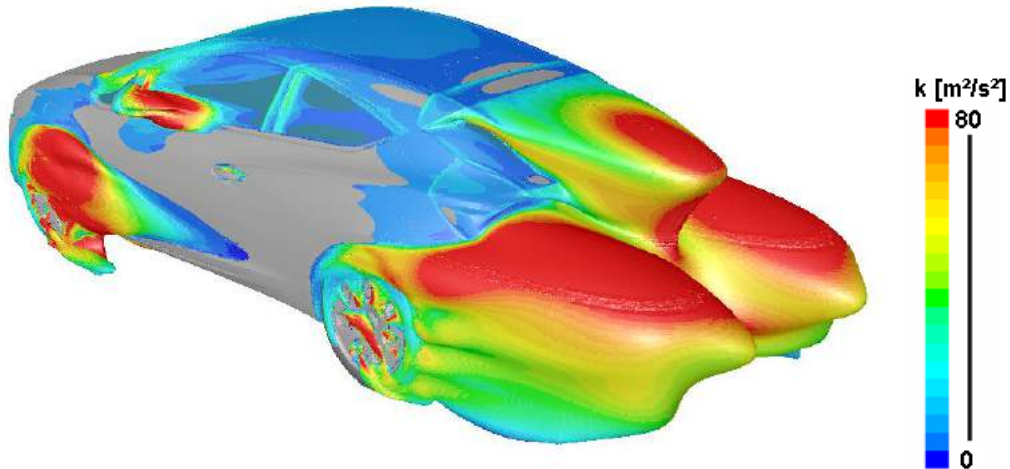


Figure 6: Simulation results (*RANS*) of the complete vehicle model. 3D isosurface of the mean total pressure $\langle p \rangle = 0 \text{ bar}$.

All boundary surfaces of the virtual wind tunnel (INLET, OUTLET, SIDE1, SIDE2, GROUND and TOP) are identified in Figure 2. At the INLET the velocity was set to a constant value of 140 kph. At the OUTLET a pressure outlet condition is applied. The symmetry condition is used on the TOP as well

as on SIDE1 and SIDE2 surfaces. In order to approximate the rotation of the wheels at steady state the Multiple Reference Frame Model (MRF) was used. At the GROUND surface a moving wall condition was applied. All other surfaces of the model are set to the non-slip condition using the non-equilibrium wall function since the first cell was placed in the log-layer obtaining typical values of $y^+ \approx 30$ (see Figure 4).

3.2 Numerical results

The flow field around the vehicle is illustrated in Figure 5. The flow is characterized by a big stagnation point at the front part of the vehicle and a smaller one at the windshield. Low velocity values are depicted in the airflow through the engine compartment and underbody as well at the wake of the vehicle as shown in Figure 5a.

The location of the main turbulent structures are identified by the isosurface of the total mean pressure $\langle p \rangle = 0 \text{ bar}$ as illustrated in Figure 6. The isosurface is colored by the Turbulent Kinetic Energy k and shows that the main structures originate from each wheel (4 Structures), each sidemirror (2 Structures) and from the rear end of the vehicle (1 Structure).

4. Submodel

In order to simulate the three dimensional and unsteady turbulent characteristics of one of the 7 turbulent structures depicted in Figure 6 a submodel is defined. The submodel definition encloses the rear upper part of the vehicle geometry as shown in Figure 7a.

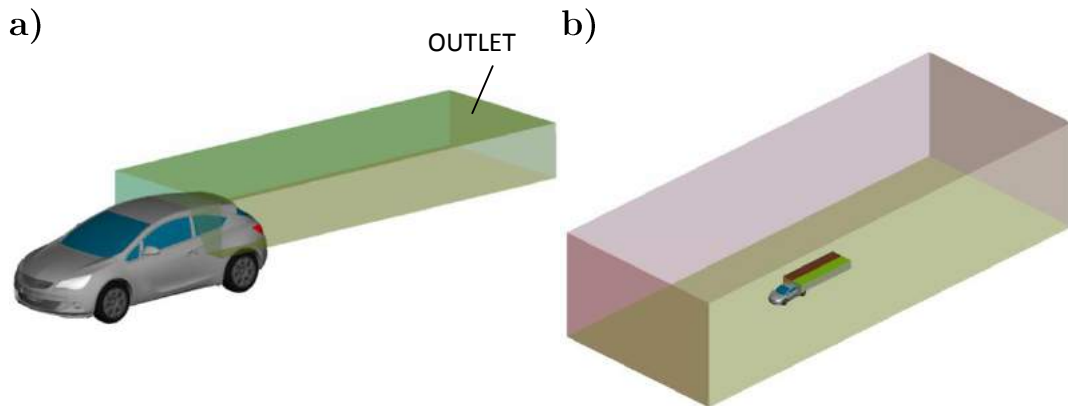


Figure 7: Computation domain of the submodel. a) Boundaries of the submodel's domain colored as translucent green surfaces. b) Comparison size of the submodel with the wind tunnel dimensions.

In the mainflow direction the subdomain is beginning near the B-pillar of the vehicle, while perpendicularly to the ground the domain is beginning just below the tail lamps. The submodel domain is 7m long, 2.6m wide and 0.15m high. A comparison of the domain size of the complete vehicle model and the submodel is depicted in Figure 7b.

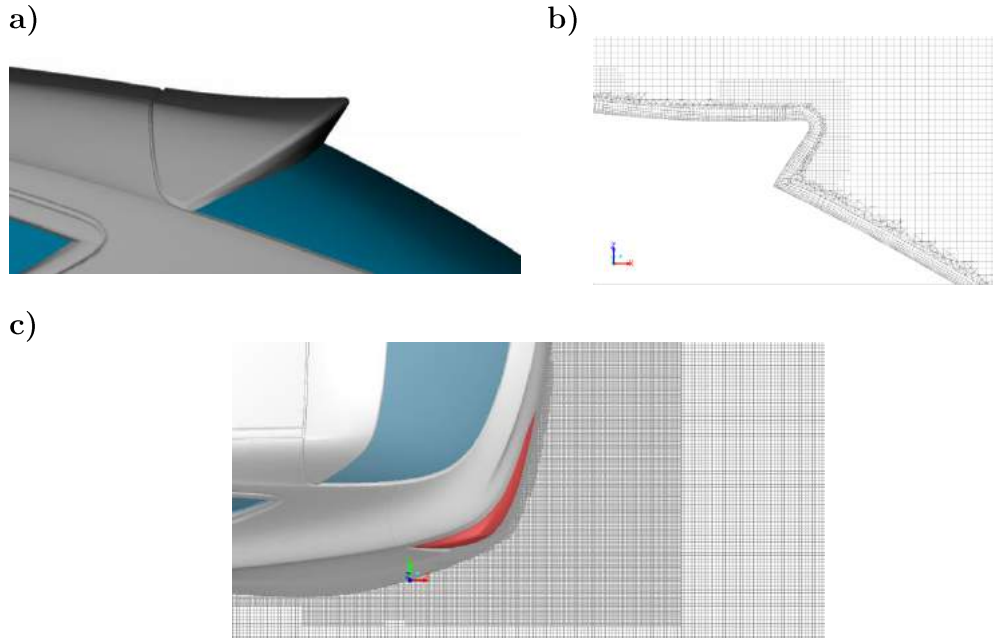


Figure 8: Geometry and computational domain of the submodel. a) Lateral view of the rear roof spoiler of the vehicle. b) X-Z plane of the numerical mesh near the roof spoiler region at the middle of the vehicle. c) X-Y plane of the numerical mesh near the rear part of the vehicle at the height of the tail lamps.

4.1 Numerical method

For the submodel a transient simulation was performed using the DES model. The numerical mesh (Figure 8b, 8c) used for the subregion (Figure 7a) is extracted from the mesh used for the complete vehicle model (Figure 2).

A pressure outlet condition was applied at the OUTLET surface. At all other boundary surfaces of the subdomain all three mean velocity components and the turbulence variables k and ε are retrieved from the full vehicle model and given explicitly as inlet conditions.

4.2 Numerical results

The non-stationary movement of the turbulent structures created at the rear upper part of the vehicle was captured by isosurfaces of the vorticity $\omega=1400$

1/s as shown in Figure 9a and 9b. In figure 9a three different turbulent structures are identified.

The origin of the first one is the central part of the rear roof spoiler. This structure is elongated parallel to the border of the spoiler and is transported through the flow to regions of higher velocity magnitude. Further upstream this big structure is breaking up into smaller ones as depicted in Figure 9b.

The second structure originates in the corner of the rear roof spoiler, while the third one originates in the slightly curved area between the rear window and the tail lamp. Both structures are aligned with the main flow direction and especially the third one is elongated in the same direction.

Comparing Figure 9a and 9b it is visible that the frequency of the movement of the three structures is different. The structure 2 and structure 3 exhibit a higher level of vorticity as recognizable in Figure 9c.

5. The need of exascale capabilities

The deep understanding of the external aerodynamics of a vehicle is a key topic for a successful automotive design since it influences the vehicle efficiency and the ride stability. The airflow over bluff bodies in the vehicle like the sidemirror, wheels or the rear roof spoiler are characterized through three dimensionality and an unsteady turbulent flow field.

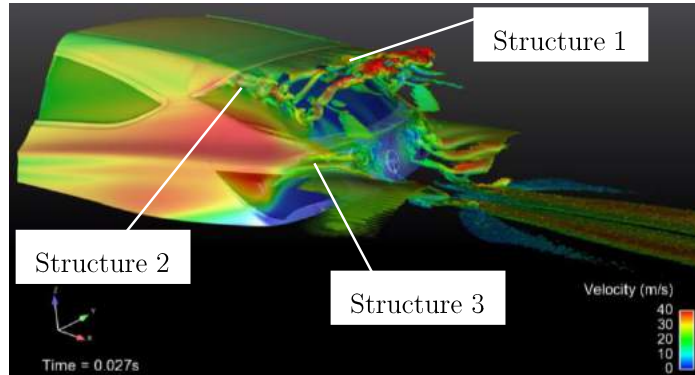
A Reynolds Averaged Navier-Stokes (RANS) approach is able to predict important engineering quantities as the mean flow field, the lift and drag coefficients. However RANS methods have difficulties with the accurate prediction of flow phenomena found around bluff bodies like vortex shedding, flow separation, reattachment and recirculation zones since the influence of the vortices are completely modeled. In the Detached Eddy Simulation (DES) approach, the unsteady RANS models are applied in the boundary layer in order to model the turbulent effects, while the Large Eddy Simulation (LES) treatment is employed to the separated regions in order to resolve the fully three-dimensional turbulent movement of the big eddies.

Simulating the turbulent flow increases the accuracy of the flow prediction, however the CPU requirements of its calculation also increase. The total run time of the RANS calculation of the complete vehicle model (95 million mesh cells) using 95 cpus was 24 hours. For the DES simulation (timestep=0.0001s, totaltime=0.4s) of the rear vehicle submodel (29 million mesh cells) the total runtime was 8 days with the use of 192 cpus.

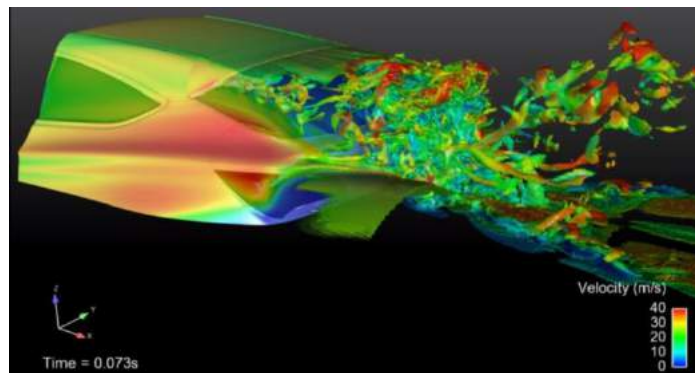
In order to have fast turnaround times (<36 hours) using the numerical

approaches that completely resolve the turbulent scales of a submodel domain or a complete vehicle model domain the exascale capabilities are required. This needs to be demonstrated with an ExaFLOW code.

a)



b)



c)

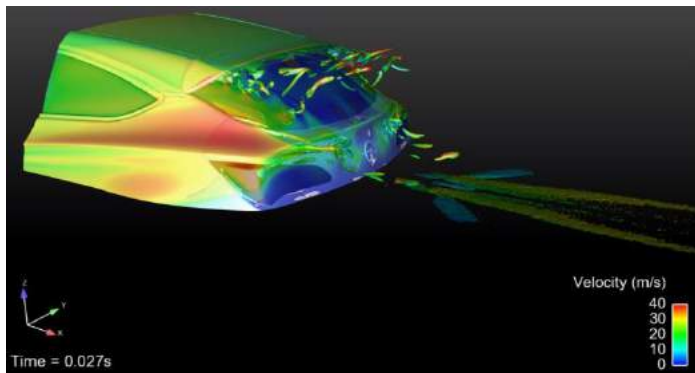


Figure 9: Simulation results (*DES*) of the submodel. a) Isosurface of the vorticity ($\omega=1400$ 1/s) at $t=0.027\text{s}$ colored by the velocity magnitude. b) Isosurface of the vorticity ($\omega=1400$ 1/s) at $t=0.073\text{s}$. c) Isosurface of the vorticity ($\omega=2300$ 1/s) at $t=0.027\text{s}$.

ExaFLOW use cases: Wing tip vortex, Imperial Front Wing and McLaren front section

J. F. A. Hoessler, J.-E. W. Lombard, S. Dhandapani, S. J. Sherwin

May 17, 2016

Abstract

This document will list three cases proposed for the ExaFLOW project, by ascending order of geometric complexity. The first, simplest case, referred in the following as the wing-tip vortex case, was introduced by Chow *et al.* (1997). The second, based on the McLaren 17D race car, was introduced by Pegrum (2006) and referred as the Imperial Front Wing. Finally, the McLaren front section is proposed as a final demonstration case of the steps towards exascale computing to be achieved by the consortium.

1 Introduction

1.1 Wing tip vortex

The wing tip vortex was studied experimentally by Chow *et al.* (1997), and later numerically, amongst other sources, by Jiang *et al.* (2008); Lombard *et al.* (2015), albeit at reduced Reynolds numbers. An advantage is the relative simplicity of the geometry, hence allowing the use of block-structured meshes (Jiang *et al.* (2008)): simulation could thus be achieved using two of the codes available, *Nek5000* and *nektar* + +.

1.2 Imperial Front Wing

The second test case under consideration is based on the McLaren 17D race car, and was studied experimentally by Pegrum (2006), hence providing validation data for the simulations. After describing the geometry (3.1) and the wind tunnel setup (3.3.1), a short description of the vortical system shed by the front wing is given, before detailing possible configurations (3.5) of increasing complexity. Detached Eddy Simulations (DES) results are referenced in order to provide rough estimates of the resolution and averaging times required to perform such simulations.

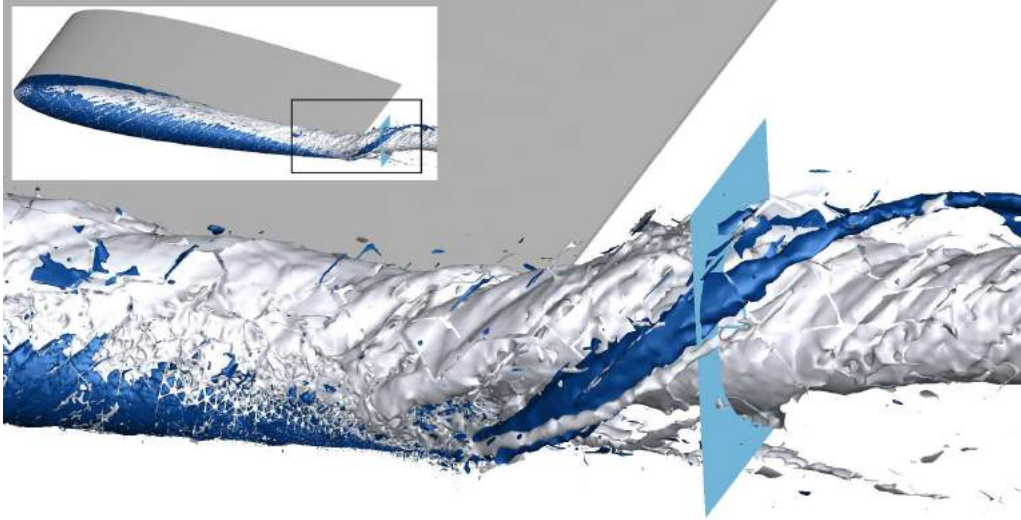


Figure 1: Contours of isohelicity showing interaction between primary and secondary wing-tip vortices Lombard *et al.* (2015)

2 Wing tip vortex

2.1 Geometry

The geometry for this test case includes a rectangular half-wing, of aspect ratio 0.75, with a NACA 0012 profile and a rounded wingtip mounted in a wind-tunnel section at an angle of attack of 10 degrees.

2.2 Experimental setup and boundary conditions

The numerical computations aim to reproduce the experimental setup where the wind-tunnel was operated such that the chord Reynolds number $Re_c = 4.6 \times 10^6$. Numerical computations differ from experiment in that the wind-tunnel walls are treated as slip boundary conditions. A uniform inflow velocity is prescribed at the inflow and details regarding the outflow boundary condition can be found in Lombard *et al.* (2015).

2.3 Benchmark case for quantifying development progress

The geometry in CAD format, the timings, the mesh, the session file for the published case are freely available to the consortium. Additionally we have a lower resolution 4th order case as well as a higher resolved 7th order accurate computation. These can be used as benchmarks for both the improvements in computational efficiency but also in terms of flow physics modeling. Unless a full DNS is desired this case does not require an exascale machine but it is large enough case that it can be used for benchmarking incremental improvements. Table 1 provides some initial figures to characterise the performance at different polynomial order and MPI ranks ran on ARCHER as a reference.

Spatial accuracy	MPI Ranks	Time-step	Avg. CPU time/time-step	Global DOFs
4 th	960	3×10^{-5}	0.18	1.5×10^6
6 th	1920	1×10^{-5}	0.32	6.9×10^6
7 th	1920	1×10^{-5}	0.45	11.9×10^6

Table 1: Average CPU time per time-step for the wing-tip case run on

2.4 Validation data

Chow *et al.* (1997) provides detailed characterisation of the vortex position and core axial velocity and static pressure, as well as Reynolds stresses components at different streamwise locations for the vortex core.

3 Imperial Front Wing

3.1 Geometry

The test case consists of a front wing attached to a simplified nosebox and a front wheel, as depicted in fig. 2. The outboard section of the wing sheds multiple co-rotating vortices which form a complex system (fig. 3). This system will need to negotiate an adverse pressure gradient generated by the front wheel.

3.2 Nomenclature

The front wing is a three elements cascade, respectively the mainplane, vane and flap when moving downstream, and the mainplane chord ($c = 0.25m$) along the centreline will be used in the following as reference length. The second length scale of interest is the ride-height h , namely the distance between the outboard lowest point of the wing and the ground (see red dotted line in fig. 2). The non-dimensional number h/c quantifies the ground effect on the wing, and will be used to define two distinct configurations. Finally, the averaging time required to capture accurate statistics will be based on the wheel diameter $d_w = 0.652m$, which represents the largest scale in this problem.

3.2.1 Conventions

In the following, x is the streamwise direction, y the spanwise direction, where $y = 0$ is the car centreline, and z the vertical direction. Only half of the car is represented (consistent with the experiment where a splitter plane was used at $y = 0$), and $y < 0$.

3.2.2 Model preparation

The CAD model has been recently improved to allow parametric changes of the h/c ratio (this was done experimentally by increasing the hanger height). Secondly, the wing is being resurfaced to avoid curvature discontinuities that could prove problematic for high

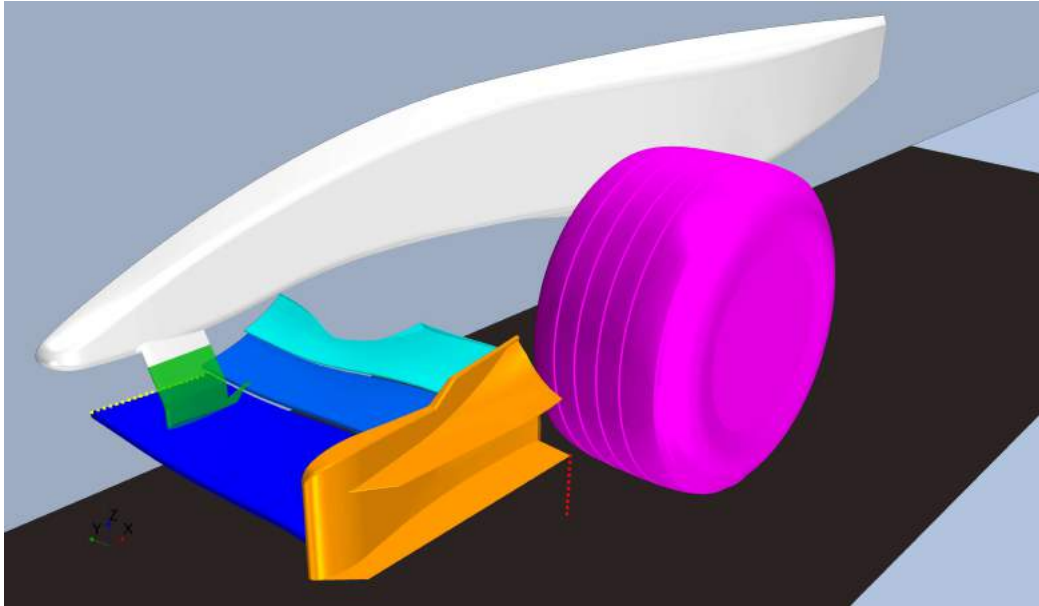


Figure 2: Use case geometry showing the ride height h (red dotted line) and chord c (yellow dotted line). Nomenclature: mainplane (blue), vane (light blue) flap (cyan), endplate (orange), hanger (green), nosebox (white), moving belt (dark gray)

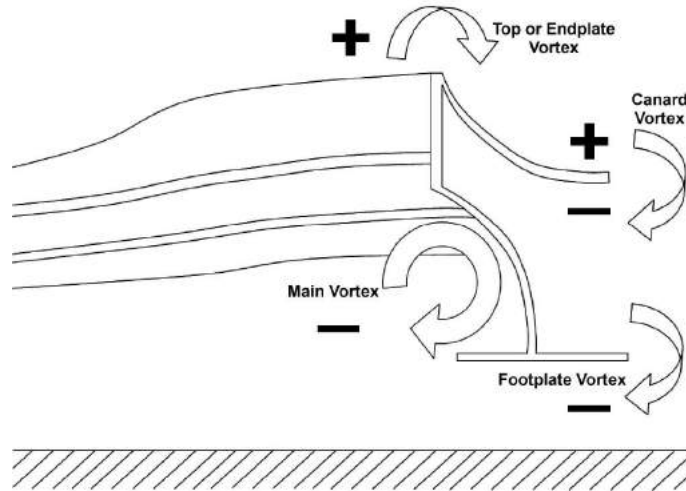


Figure 3: A schematic of the topology of the vortex system downstream of the front wing and endplate, courtesy of Pegrum (2006)



Figure 4: Tyre curtain used to model the point contact between the tyre and the ground (red), and tyre grooves (cyan)

order mesh generators, and the final model is expected to be available by the end of Spring 2016.

3.3 Run conditions

3.3.1 Experimental setup

The experimental dataset used as reference was produced at the Donald Campbell Wind Tunnel at Imperial College London using a 50% scale model. The test section is equipped of a rolling road and the maximum turbulence intensity was measured at 0.15%.

3.3.2 Tyre/ground contact point

During the experiment, no active load was applied to the wheel, which is therefore undeformed.

To represent in the simulations the point connection between the tyre and the ground, the standard approach is to use a tyre curtain (see fig. 4) which will be one of the key details in obtaining accurate tyre wake shape. Its height, shape and mesh resolution will also be a limiting factor for time step selection as the inboard side of that curtain is the region of peak velocity (typically $\approx 2U_\infty$).

Secondly, the tyre used in the experiment was grooved (see fig. 4). The influence of those groove is being quantified by McLaren and the model provided will be available with and without this feature. Croner (2014) reported, on different grooves depth-to-width ratio, a jetting of nearly $2U_\infty$ within said grooves near the tyre curtain, and showed they had a significant impact on both drag and wake structure.

3.4 Boundary conditions

The use case model is at full scale, and thus to maintain an equivalent blockage to the experiment, the simulation test section is of $W = 2.68m$ by $H = 2.44m$. The Reynolds number Re_c based on chord length c and the free stream velocity U_∞ is $Re = 2.0 \times 10^5$. The boundary conditions are as follows:

- wing and nosebox are walls

h/c	<i>Origin</i> (mm)	e_0	e_1	e_2
0.36	[39.2, -879.4, 320.9]	[1, 0, 0]	[0, -0.4362, 0.99905]	[0, -0.99905, 0.04362]
0.56	[38.3, -879.4, 271.0]	[1, 0, 0]	[0, -0.4362, 0.99905]	[0, -0.99905, 0.04362]

Table 2: Wheel coordinate systems for both h/c ratios

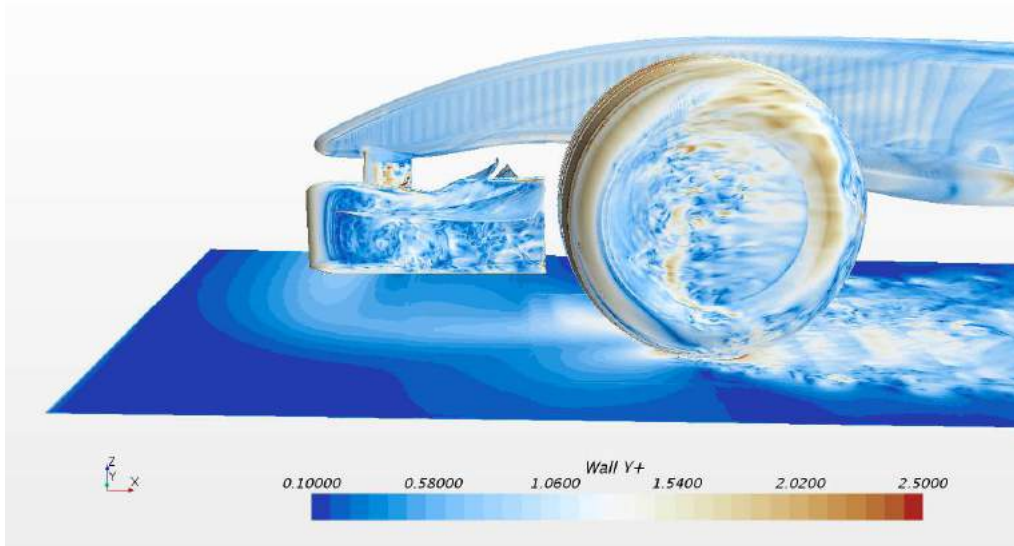


Figure 5: Instantaneous y^+ distribution for a first cell height $l/c = 2 \times 10^{-4}$

- The tyre rotates along the e_2 vector of the coordinate systems defined in table 2
- The ground has a prescribed velocity $[U_\infty, 0, 0]$ (moving belt)
- A uniform velocity profile is used at the inlet as the boundary layer suction and moving belt guarantee a negligible boundary layer buildup before reaching the model
- The ceiling and far side should be treated as symmetry planes
- Symmetry plane at $y = 0$

At the considered Re_c , the typical first cell height to obtain a $y^+ \approx 1$ should be set at $l/c \approx 2 \times 10^{-4}$ on all surfaces (see fig. 5 for a snapshot of y^+ on the model):

3.5 Proposed configurations

3.5.1 Isolated wing

The front wing endplate sheds a system of four vortices (see fig. 3), and detailed total pressure probe surveys are available for the front wing in isolation (no front wheel) in Pegrum (2006). This could be considered as a first configuration of interest as the time-step restrictions and resolution requirements would be less severe than for the full

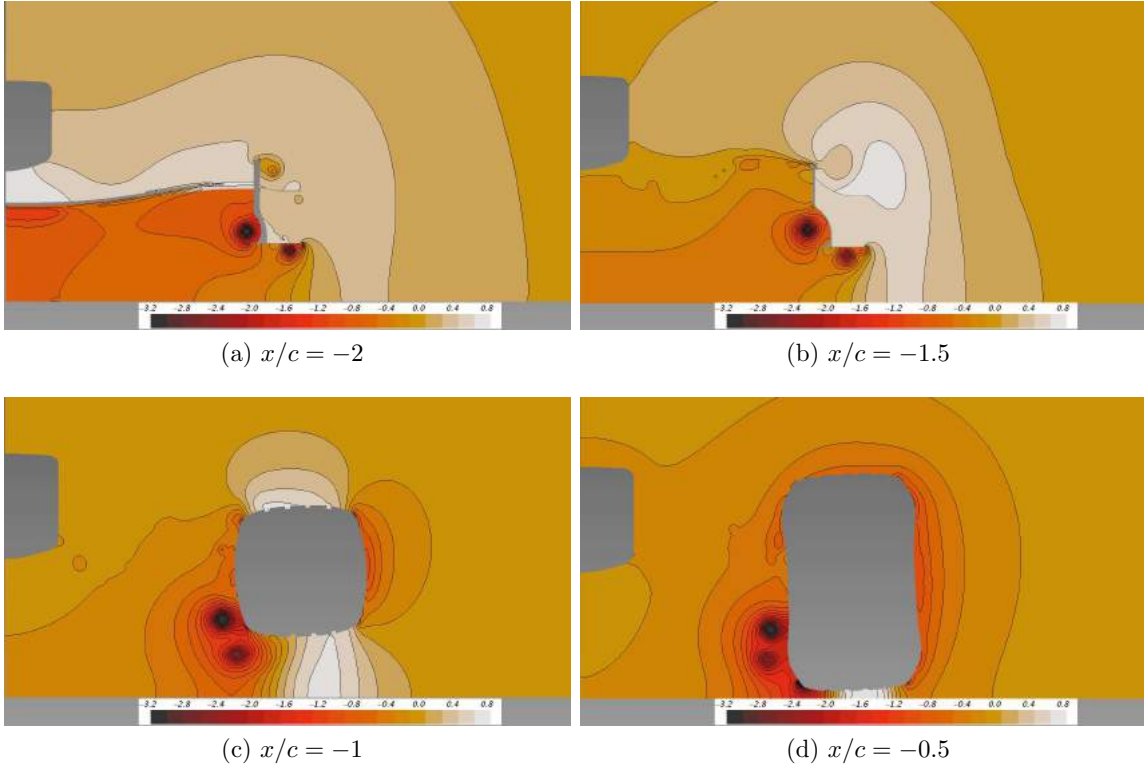


Figure 6: Contours of time averaged pressure coefficient at different x positions showing the vortex system from the front wing endplate negotiating the tyre

geometry. Detailed RANS and DES simulations at two h/c ratios (0.36 and 0.56) are being performed.

3.5.2 Isolated wheel

A second sub-problem of interest is the isolated wheel, for which a few simulations have been performed in Nektar++ prior to the ExaFLOW project.

3.5.3 Full geometry

Two h/c ratio are considered (0.36 and 0.56) and documented in Pegrum (2006), also including vortex trajectories around the tyre. Fig 6 shows a few snapshots of the time-averaged pressure coefficient when moving downstream.

3.6 Initial results

The isolated wing was run at $h/c = 0.48$ on a McLaren Cluster for three different core counts, resp. 1024, 2048 and 6144 cores for 500 iterations in order to obtain initial performance indicators. The session file and restart have been archived to ensure this simulation is reproducible, although issues with the mesh were identified. The table 3 presents those results. It is worth mentioning that the mesh in question was small

MPI ranks	Average time per its (s)
1024	5.9
2048	4.5
6144	1.5
8192	1.4

Table 3: Average time per iteration for a run of Imperial Front wing without the wheel at $h/c = 0.48$ for different core counts

enough for weak scaling to become an issue for the greatest of the three core count, and a more thorough test will be performed during August when our production cluster becomes available.

4 The need for exascale capabilities

The McLaren front section (which could be extended to a full model at full resolution) is proposed as a demonstration case for the steps towards exascale computing to be achieved during the project. To justify the need for exascale computing on this geometry, let's start by a few numbers. The free-stream velocity reached in race conditions is $U_\infty \approx 70\text{m/s}$, and the tyre length scale is $L_T \approx 0.6\text{m}$, yielding a Reynolds number $Re \approx 2.8 \times 10^6$. The scales range from 1mm based on the thinnest trailing edges to 2m for the topbody characteristic length.

On top of resolving the structures of the boundary layers present around the different lift generating devices, the geometry yields large fully separated regions in the wakes of the tyres, which interact off-body with vortical structures. Finally, vortices which are shed from the front wheel and track to the rear corner create a strong coupling between the front and rear of the car, hence activating scales of $\approx 5\text{m}$. As a consequence, obtaining statistical moments would require an averaging period of $\approx 0.6\text{s}$ assuming ≈ 10 characteristic lengths for the largest scale involved.

Secondly, from our Industry perspective, the development time scales have to be taken into consideration: the full life of one of our race cars is a year, along which four to five major upgrades and their associated change of Aerodynamics concept will be considered. Thus, for fully resolved computational Fluid Dynamics simulations to be accepted within our production process where the time scales are of the order of weeks, there is a strong need to be able to scale up the simulations

References

- CHOW, JIM S, ZILLIAC, GREGORY G & BRADSHAW, PETER 1997 Mean and turbulence measurements in the near field of a wingtip vortex. *AIAA journal* **35** (10), 1561–1567.
- CRONER, E. 2014 Etude de l'écoulement autour des ensembles roulants d'un véhicule en vue de l'optimisation aérodynamique du pneumatique. PhD thesis, Université de Toulouse.

JIANG, LI, CAI, JIANGANG & LIU, CHAOQUN 2008 Large-eddy simulation of wing tip vortex in the near field. *International Journal of Computational Fluid Dynamics* **22** (5), 289–330.

LOMBARD, JEAN-ELOI W., MOXEY, DAVID, SHERWIN, SPENCER J., HOESSLER, JULIEN F. A., DHANDAPANI, SRIDAR & TAYLOR, MARK J. 2015 Implicit large-eddy simulation of a wingtip vortex. *AIAA Journal* **54** (2), 506–518.

PEGRUM, J. M. 2006 Experimental study of the vortex system generated by a formula 1 front wing. PhD thesis, Imperial College London.